ADVANCED MATERIALS

Supporting Information

for *Adv. Mater.,* DOI: 10.1002/adma.202102883

The Role of Additives in Suppressing the Degradation of Liquid-Exfoliated WS_2 Monolayers

*Leonhard Karger, Kevin Synnatschke, Simon Settele, Yvonne J. Hofstetter, Tim Nowack, Jana Zaumseil, Yana Vaynzof, and Claudia Backes**

Supporting Information

The role of additives in suppressing the degradation of liquid-exfoliated WS_2 monolayers

Leonhard Karger,[1,≠] Kevin Synnatschke,[1,≠] Simon Settele,[1] Yvonne J. Hofstetter,[2,3] Tim Nowack,[1] Jana Zaumseil,[1,4] Yana Vaynzof, [2,3] Claudia Backes[1*]

[1]*Institute for Physical Chemistry, Heidelberg University, Im Neuenheimer Feld 253, 69120 Heidelberg, Germany*
[2]*Integrated Center for Applied Photophysics and Photonic Materials, TU Dresden, Nöthnitzer Straße 61, 01187 Dresden, Germany*
[3]*Center for Advancing Electronics Dresden (cfaed), TU Dresden, Helmhotzstraße 18, 01069 Dresden, Germany*
[4]*Centre for Advanced Materials, Ruprecht-Karls-Universität Heidelberg, Im Neuenheimer Feld 225, 69120 Heidelberg, Germany*

[≠] These authors contributed equally

*backes@uni-heidelberg.de

Content

1. Basic characterization of the WS_2 dispersions

1.1 Optical Characterization

Prior to degradation experiments, the size-selected WS_2 dispersions were subjected to basic optical characterization to assess their quality and suitability for the measurement (Figure S1). The optical extinction spectra (Figure S1A,B) show the characteristic size and thickness dependent changes.[1] In brief, edges are electronically different compared to basal planes and have a different absorbance coefficient at each wavelength. Therefore, peak intensity ratios can be used to determine the average lateral size of the nanosheets. The mean nanosheet length, <L>, can be calculated from the ratio of the extinction at 235 nm, Ext_{235}, to the extinction at 290 nm, Ext_{290}, according to equation 1.[2] Furthermore, confinement and dielectric screening effects have an impact on the exciton energies, *i.e.* peak positions.[1b, 3] The mean layer number, <N>, can be calculated from the position of the A exciton by equation 2.[2] In analogy to previous work, [1b, 2] we determined the position of the A exciton from the second derivative of the spectra, d^2Ext/dE^2, since this will partially compensate for artificial shifts caused by the scattering background.

$$< L >= \frac{2.30 - Ext_{235}/Ext_{290}}{0.02Ext_{235}/Ext_{290} - 0.0185} \quad (1)$$

$$< N >= 6.35 \cdot 10^{-32} \cdot exp(\lambda_A(nm)/8.51) \quad (2)$$

Due to the relationship between averaged layer number and monolayer content,[4] the monolayer volume fraction can also be estimated. The values are summarized in Table 1.

Overall, the optical properties of the dispersion exfoliated and size-selected in SC and SDS are similar, except for a red-shift shift in the A-exciton photoluminescence in SDS compared to SC (Figure S1E,F). This shift is attributed to solvatochromic effects from the difference in the dielectric environment in the two surfactant systems. Note that such a shift is also expected to occur in the absorbance/extinction spectra- an effect that has been reported for *N*-methyl-2-pyrrolidone as solvent.[1a] Since the metrics were established with SC as surfactant, this would lead to an overestimation of the layer number in SDS from spectroscopic metrics.

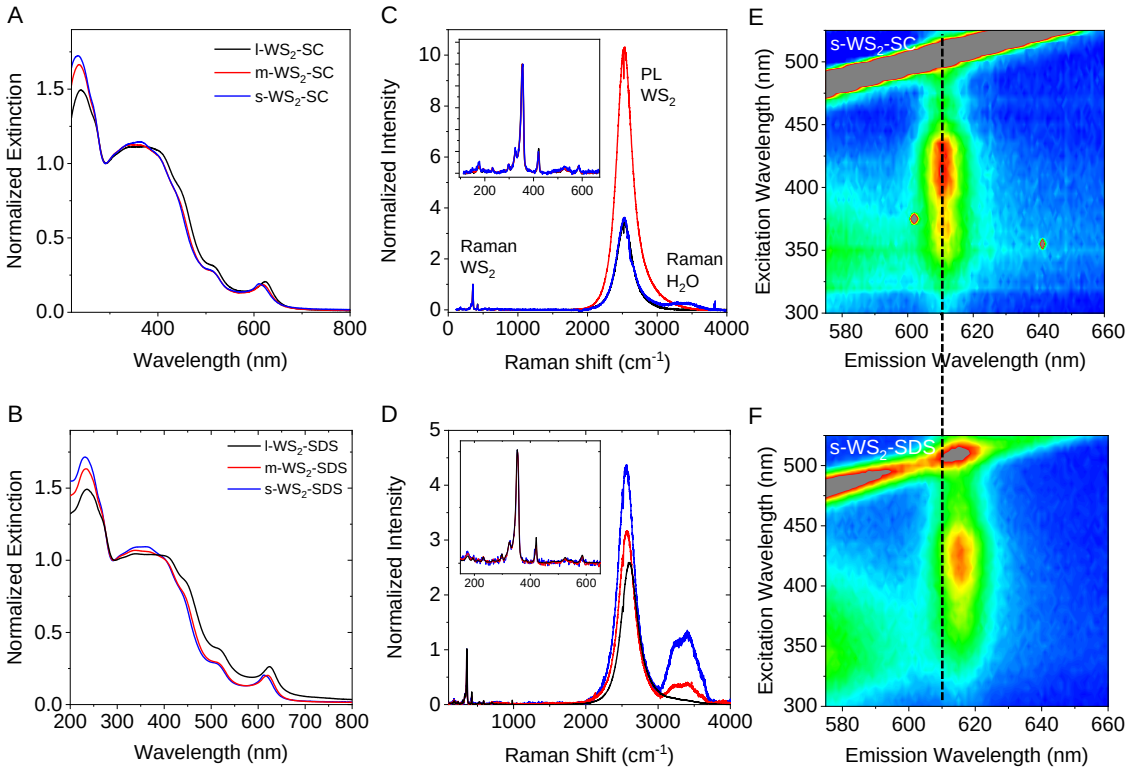

Figure S1: Basic optical characterization of the size-selected WS_2-SC dispersions. A,B) Optical extinction spectra of the size-selected fractions in SC (A) and SDS (B). C-D) Raman spectra (excitation 532 nm) showing the characteristic WS_2 Raman modes (inset) as well as the photoluminescence of the WS_2 monolayers and weak features of the water Raman of the samples in SC (C) and SDS (D). E,F) Photoluminescence-excitation contour plot of s-WS_2 measured at 20°C showing the characteristic A-exciton emission as vertical emission feature centered at ~612 nm in SC (E) and 616 nm in SDS (F). The grey feature is the water Raman.

Table S1: Average lateral size (<L>), layer number <N> and monolayer volume fraction (ML_{Vf}) of the WS_2 nanosheets in the size-selected dispersions estimated from spectroscopic metrics. Note that the metrics were established using SC as surfactant and solvatochromic shifts in SDS may lead to an overestimation in SDS (denoted by *). Therefore, the monolayer volume fraction was not estimated from <N>.

	<L> (nm)	**<N>**	**ML_{Vf}**
SC			
WS_2 1-5k *g*	73	4.4	0.02
WS_2 5-10k *g*	43	2.9	0.1
WS_2 10-30k *g*	36	1.5	0.5
SDS			
WS_2 1-5k *g*	71	5.2*	
WS_2 5-10k *g*	47	3.5*	
WS_2 10-30k *g*	38	2.0*	

1.2 Atomic Force Microscopy

For morphological characterization, the dispersions after LCC were diluted with water and deposited on APTS-coated Si/SiO_2 through dip-coating (see methods) and subjected to atomic force microscopy (AFM). This deposition method has the advantage that the solvent does not dry on the substrate resulting in a homogeneous coverage with minimal contamination and aggregation. Since this work focuses on using the photoluminescence of WS_2 monolayers to track degradation, small and thin nanosheets were isolated so that it is important to minimize contamination.

AFM images of the size-selected nanosheets in SC and SDS are shown in Figures S2 and S3, respectively. While the nanosheets are small, they often have characteristic features and shapes, such as sharp edges. The dimensions are in line with the estimate from optical extinction spectroscopy.

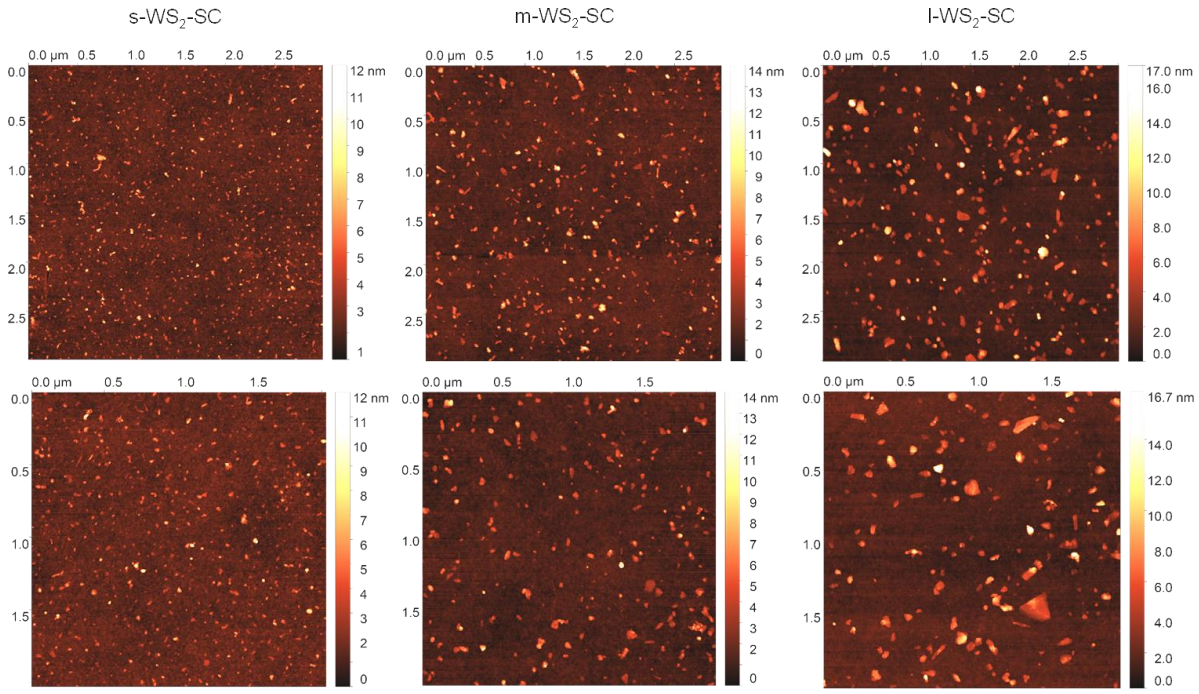

Figure S2: AFM of the WS_2 nanosheets obtained from exfoliation in SC. Left: s-WS_2 isolated as supernatant after centrifugation at 10k *g* and sediment after 30k *g*. Middle: m-WS_2 trapped between 5 and 10k *g*. Right: l-WS*2* trapped between 1-5k *g*.

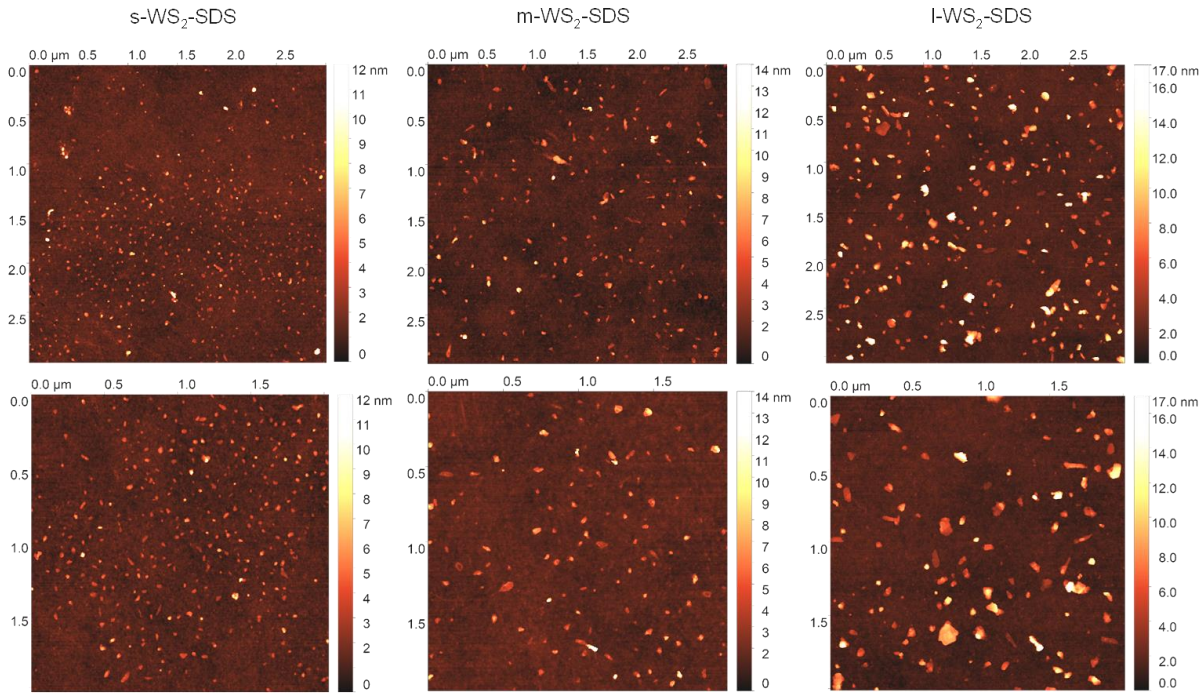

Figure S3: AFM of the WS_2 nanosheets obtained from exfoliation in SDS. Left: s-WS_2 isolated as supernatant after centrifugation at 10k *g* and sediment after 30k *g*. Middle: m-WS_2 trapped between 5 and 10k *g*. Right: l-WS*2* trapped between 1-5k *g*.

On the cursory glance, no striking difference in the morphology, lateral size and thickness of the nanosheets prepared and SC and SDS is observed. However, when examining the thinnest sheets in the samples, a difference between the two stabilizers can be observed as illustrated in Figure S4.

In SC, the thinnest sheets have an apparent AFM height of 2.5-3 nm. Even though this is much thicker than monolayers of micromechanically-exfoliated TMDs, a correlation with PL spectroscopy has previously revealed that these are indeed monolayers.[1a, 5] The increased apparent AFM height is attributed to residual solvent and surfactant. In SC, the thickness is relatively homogeneous over the nanosheet in the case of the thinnest objects (that do not have steps or terraces) as exemplarily shown by the image of m-WS_2-SC in Figure S4A and the corresponding line profile in Figure S4B. In contrast, the majority of the thinnest flakes from exfoliation in SDS have a rim of elevated thickness (0.7-1 nm) on the flake edges and the basal plane area typically has an AFM thickness of 1.5-2 nm. An example is shown in Figure S4C, D.

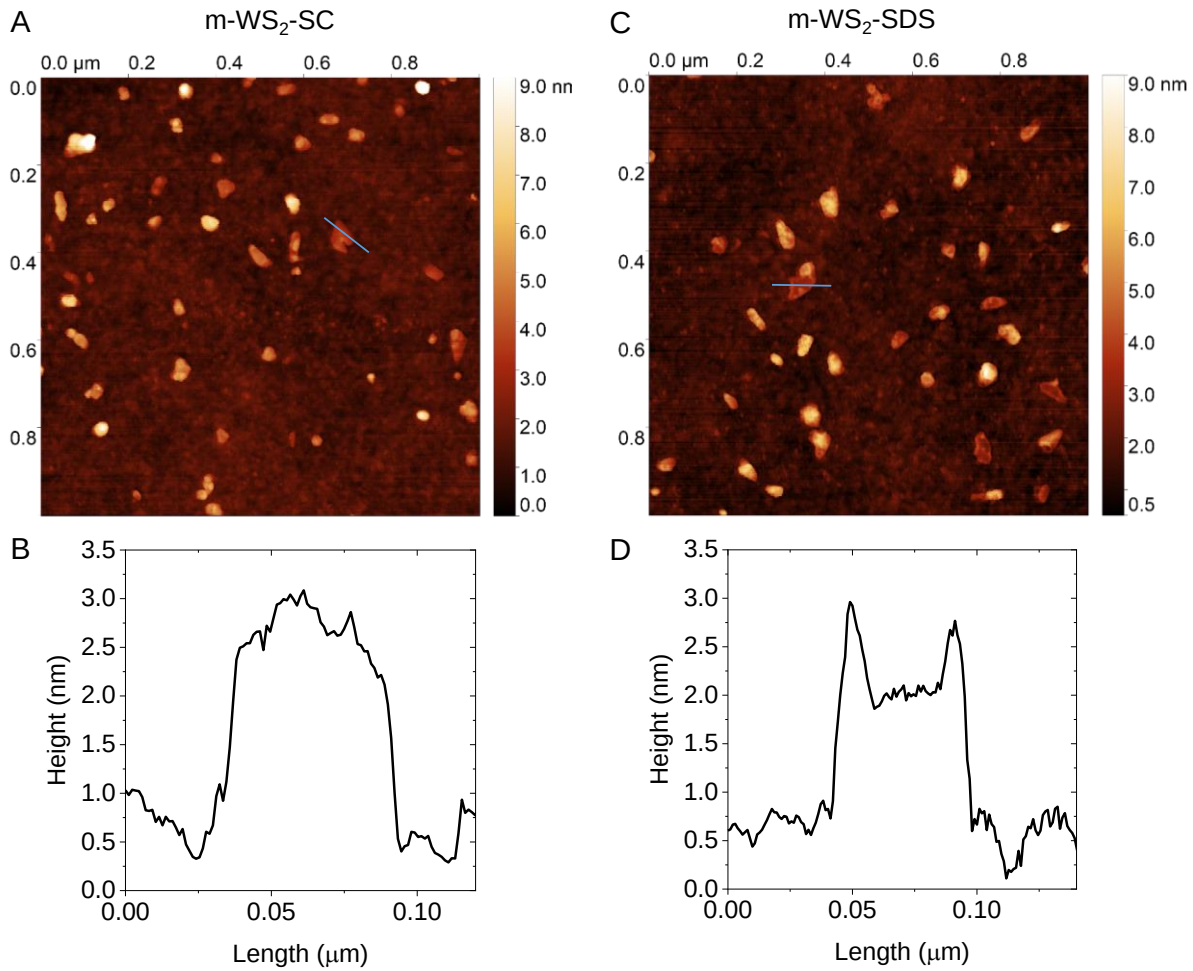

Figure S4: AFM of WS_2 nanosheets obtained from exfoliation in SC and SDS in comparison. A) AFM image of m-WS_2-SC with a representative line profile across one of the thinnest nanosheets in (B). C) AFM image of m-WS_2-SDS with a representative line profile across one of the thinnest nanosheets in (D).

The result of a statistical analysis of m-WS_2-SC and m-WS_2-SDS is displayed as scatter plot of lateral size as function of thickness in Figure S5. This clearly illustrates that monolayers have a lower apparent AFM thickness on the basal plane when using SDS as stabilizer compared to SC. Since the samples were diluted with water prior to deposition (to surfactant concentrations of < 0.05 g/L) this could suggest that desorption of SDS on the nanosheet basal plane occurs more readily than on the edges and that desorption does not occur under these conditions in the case of SC. This in agreement with previous work that showed that SC can shield LPE WS_2 monolayers from an oxidation with chloroauric acid.[6]

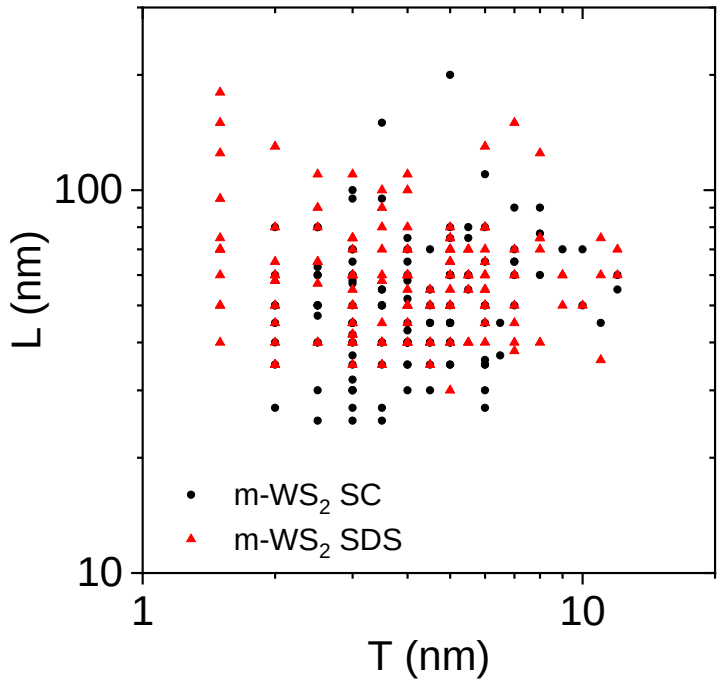

Figure S5: Statistical analysis of nanosheet dimensions from AFM of m-WS_2-SC and m-WS_2-SDS shown as scatter plot of longest dimension as function of apparent AFM thickness. Each data point represents an individual flake. For nanosheets with an apparent rim of elevated thickness at the edges, the thickness was determined from the basal plane area.

2. PL temperature ramps of WS_2-SC

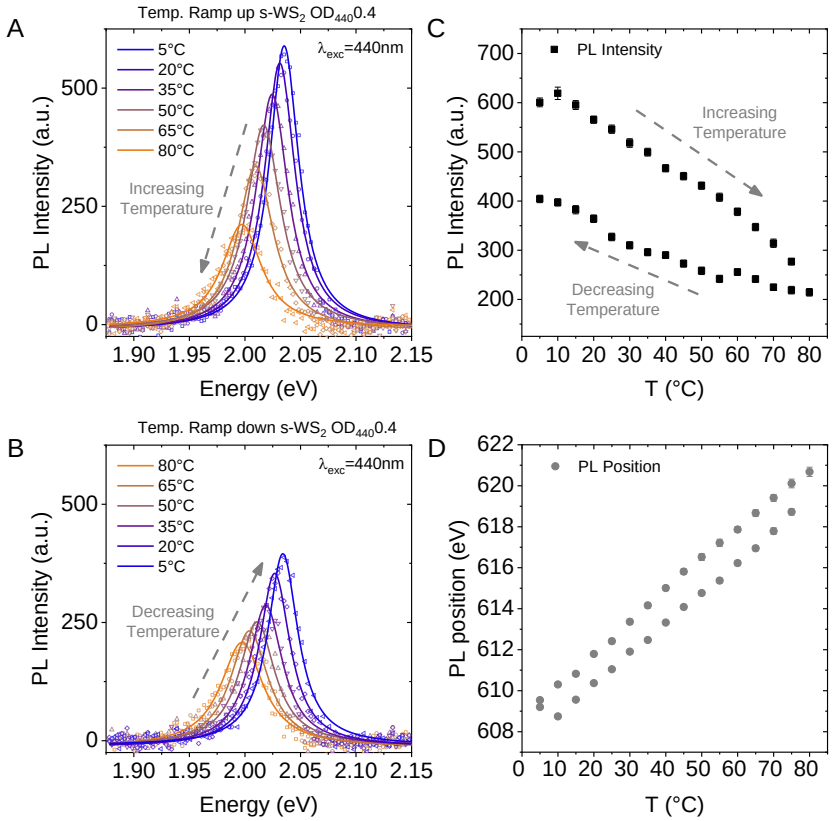

Figure S6: Temperature-dependence of the A-exciton photoluminescence of s-WS_2-SC. The temperature was increased in 5°C increments from 5°C to 80°C and then decreased again to 5°C. Prior to each measurement, the temperature was held for 5 min. A-B) PL spectra (440 nm excitation) of the ramp increasing the temperature (A) and decreasing the temperature (B), respectively. All spectra can be described well by a single Lorentzian fit (solid lines). C-D) Plots of PL intensity (C) and position (D) as function of temperature.

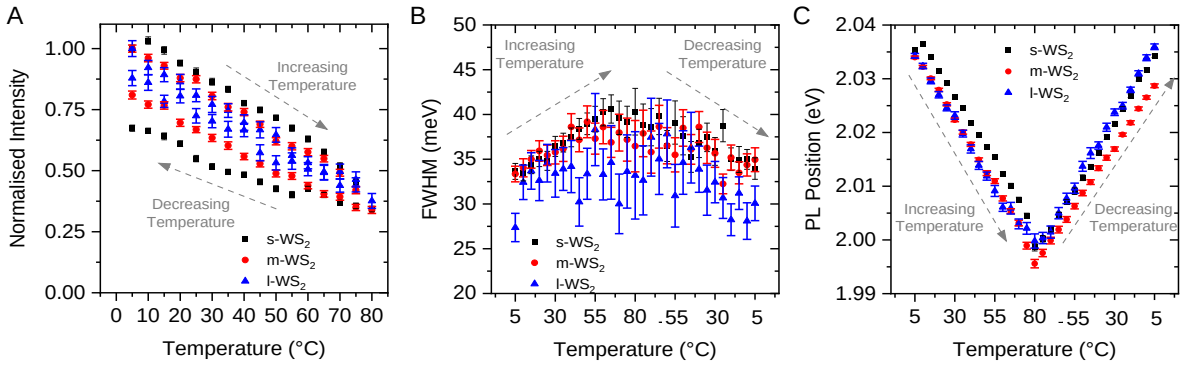

Figure S7: Temperature-dependence of the A-exciton photoluminescence of size-selected WS_2-SC. The temperature was increased in 15°C increments from 5°C to 80°C and then decreased again to 5°C. Prior to each measurement, the temperature was held for 5 min. A) PL intensity normalized to the initial measurement, B) full width at half maximum and C) PL position as function of temperature extracted from fitting the PL spectra to a single Lorentzian. Error bars are errors of the fit.

3. Degradation kinetics

3.1 WS_2-SC

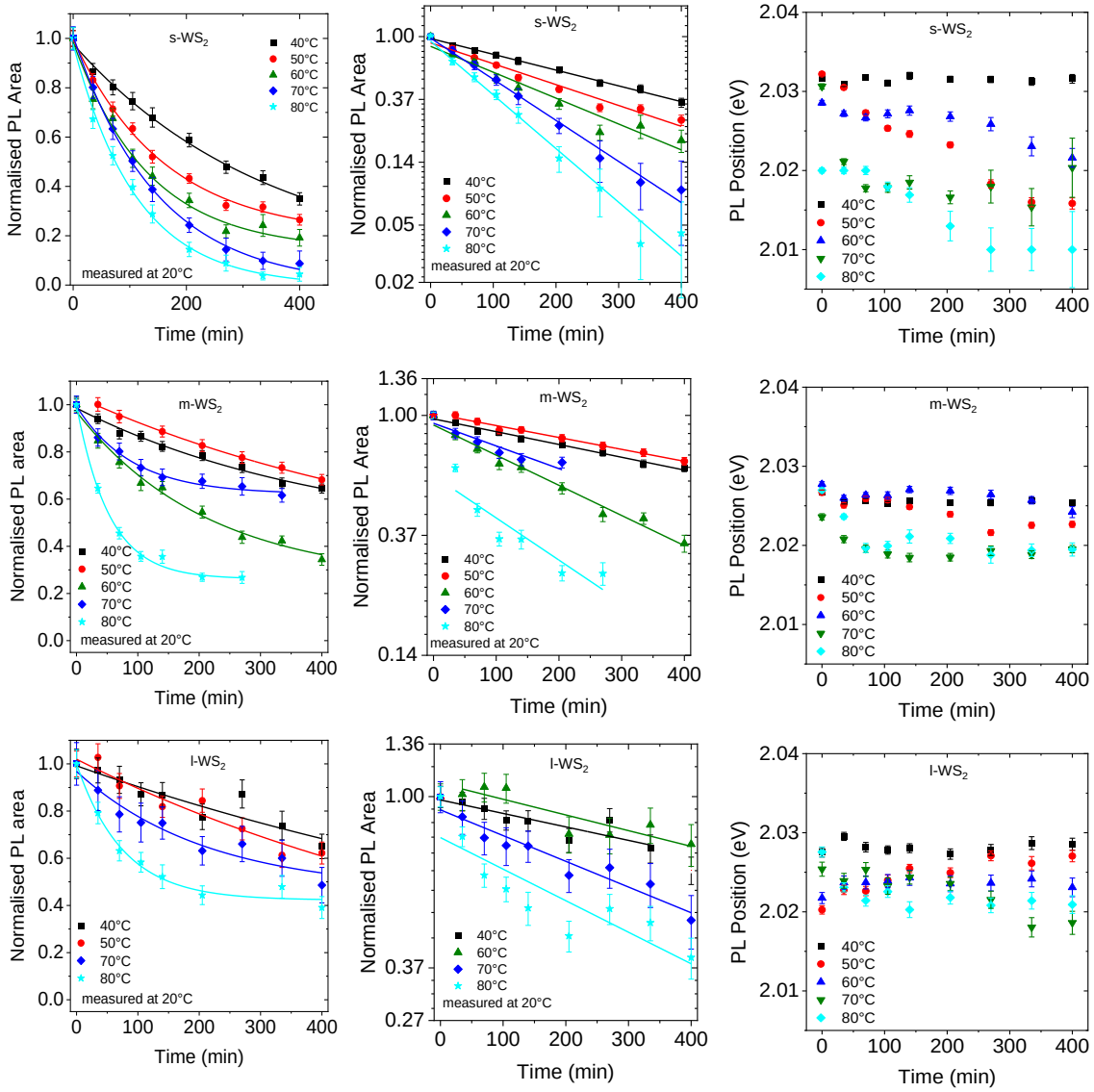

Figure S8: PL degradation kinetics of size-selected WS_2-SC measured at 20°C after heating and irradiation to the temperatures indicated in the figure legend. Top: s-WS_2, middle: m-WS_2, bottom: l-WS_2. From left to right: Normalized PL area as function of time on a linear scale fitted with a single exponential, normalized PL area on a semi-logarithmic scale fitted with a linear regression, PL position as function of time.

As shown in figure S9 the PL emission position of s-WS_2-SC shows a red shift with increasing irradiation and heating in some of the datasets. Note that this is not apparent in the case of m-WS_2 and l-WS_2. Below we discuss potential explanations for this shift, but note

that the photoluminescence of mono-layered TMDs is influenced by many factors so that the interpretation needs to be taken with care.

Red-shifted PL-emission can be caused by trion emission, as is observed in some of the microscopic studies. However, the expected energy range for such emissions would be much lower.[7] Furthermore, the data can still be fit well with a single Lorentzian and no systematic increase in the line width is observed which would be expected if the red-shift was due to an increased emission from trions.

Instead we believe that the degradation introduces near edge intra-gap states through change in the local chemical composition, *e.g.* oxygen substitution, which could result in more subtle red-shifts.[8] With decreasing nanosheet size these effects become more pronounced, which could be caused by preferential formation of such features on the edges. This agrees with findings by Atkin *et al.* who observe red-shifted PL near to WS_2 nanosheet edges upon irradiation.[9] Further, the PL position shift would be more pronounced when the overall degree of degradation is higher which is the case in the s-WS_2 dataset.

Note that a similar red shift is not observed in the SDS stabilized WS_2 (Figure S10), although the PL positions varies across the datasets intrinsically. This could be caused by the additional thermal decomposition in s-WS_2-SDS potentially leading to different degradation products which do not influence the band gap significantly.

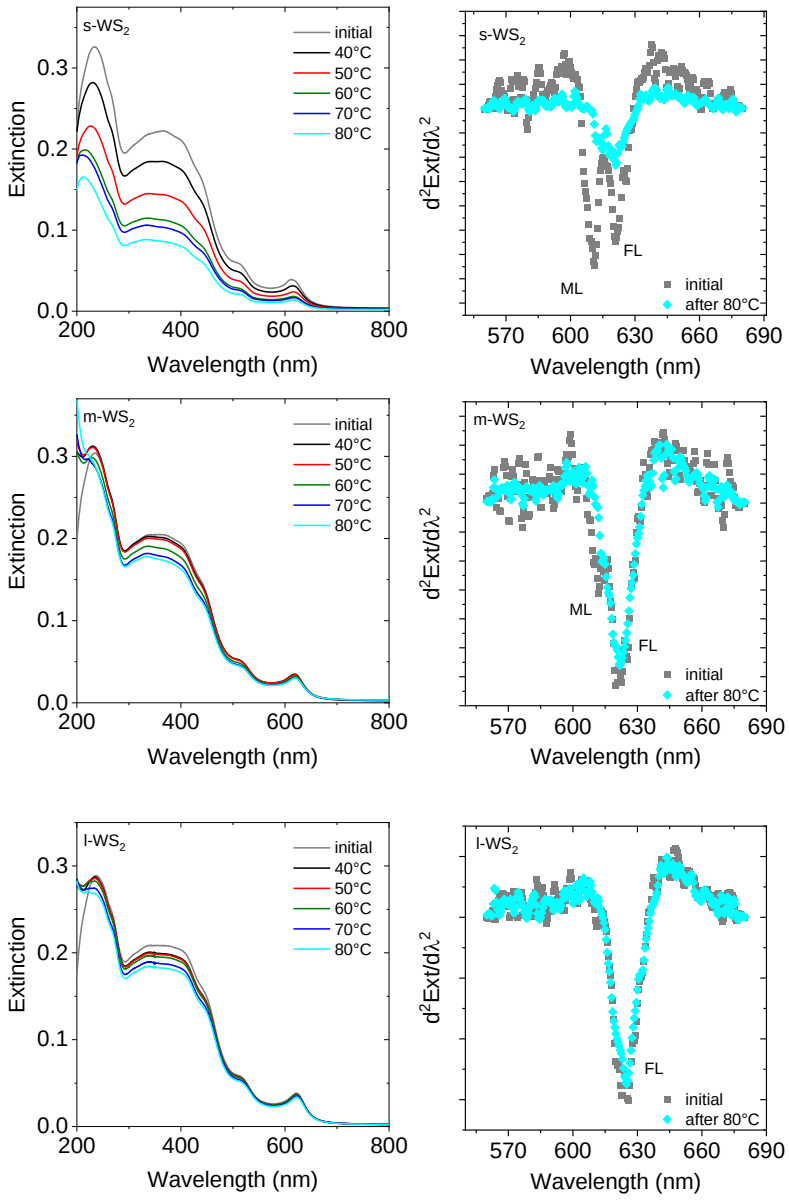

Figure S9: Extinction spectra of size-selected WS_2-SC after heating/irradiation to the temperatures indicated in the figure legend for 400 min. Top: s-WS_2, middle: m-WS_2, bottom: l-WS_2. Left: Extinction spectra, right: second derivative of the A-exciton of the initial samples and sample heated/irradiated at 80°C. For s-WS_2 the degradation can be observed from a drop in extinction intensity, while for m-WS_2 and l-WS_2, the changes are minor. In the A-exciton region, the monolayered (ML) and few-layered (FL) WS_2 can be observed. In particular the monolayer component decreases in intensity after heating/irradiation suggesting preferential degradation of monolayers. The minor drop in extinction intensity of m-WS_2 and l-WS_2 is consistent with this interpretation since the monolayer volume fraction is significantly lower (see Table S1) so that the overall extinction is dominated by few-layered WS_2 in these samples.

3.2 WS_2-SDS

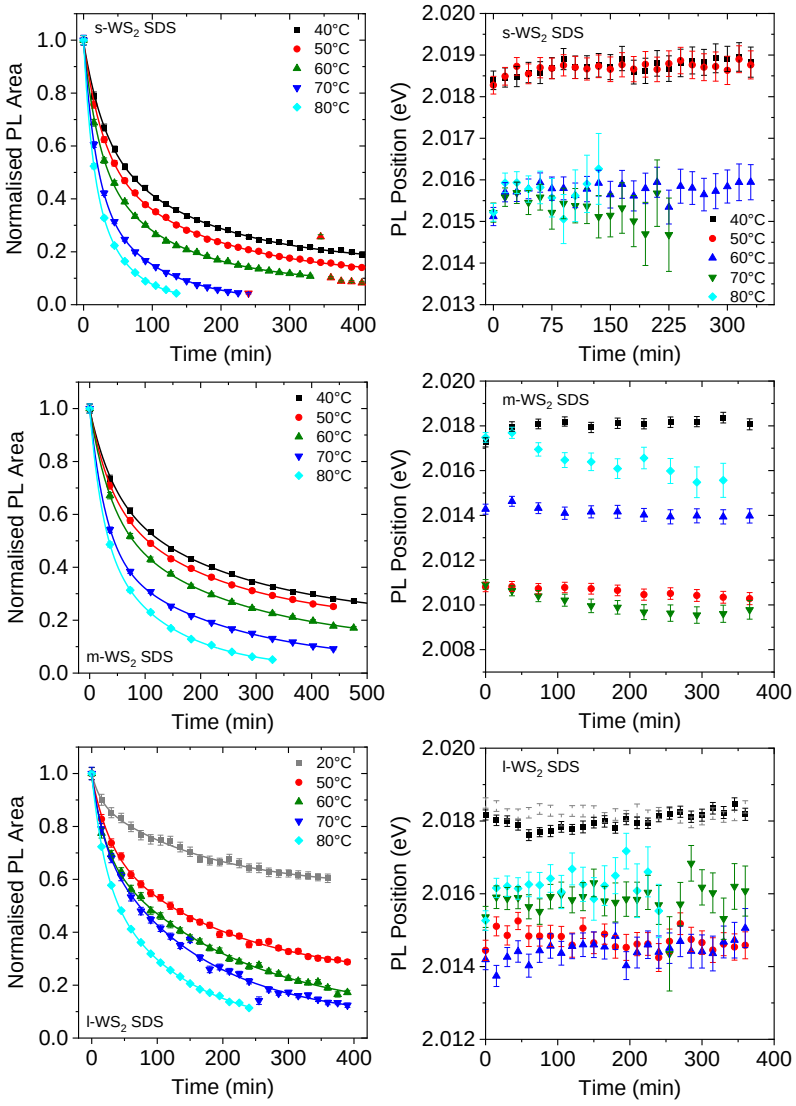

Figure S10: PL degradation kinetics of size-selected WS_2-SDS measured at 20°C after heating and irradiation to the temperatures indicated in the figure legend. Top: s-WS_2, middle: m-WS_2, bottom: l-WS_2. Left: Normalized PL area as function of time on a linear scale fitted with a biexponential. Right PL position as function of time.

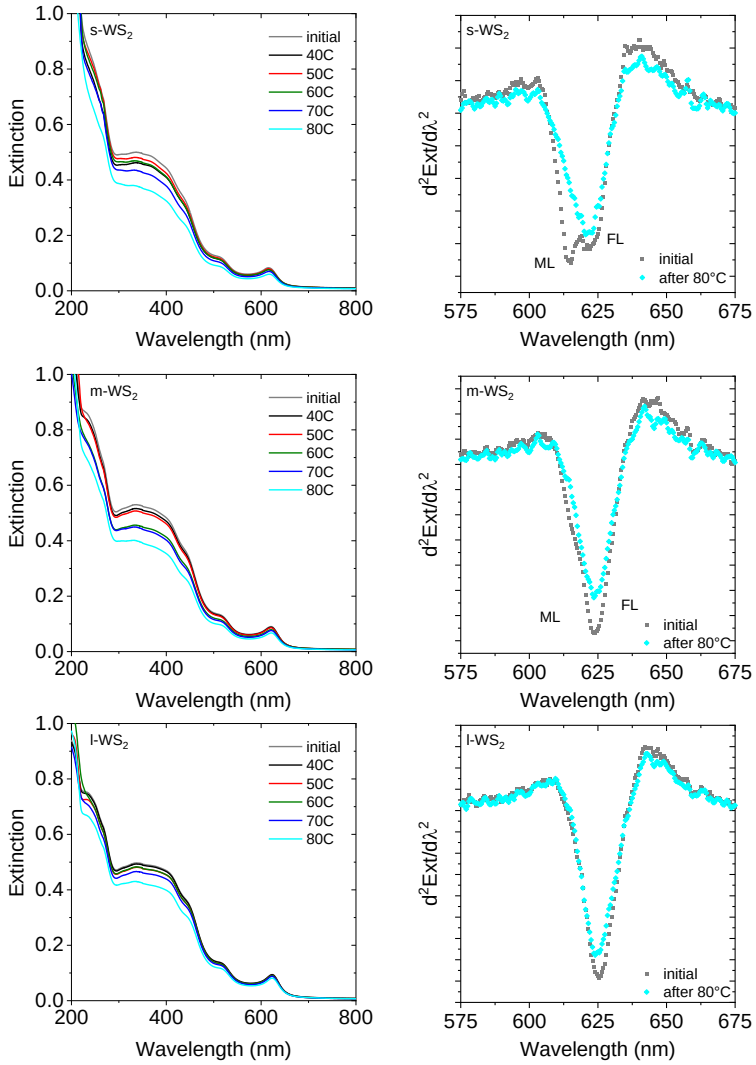

Figure S11: Extinction spectra of size-selected WS_2-SDS after heating/irradiation to the temperatures indicated in the figure legend for 400 min. Top: s-WS_2, middle: m-WS_2, bottom: l-WS_2. Left: Extinction spectra, right: second derivative of the A-exciton of the initial samples and sample heated/irradiated at 80°C.

4. Characterization of the degradation products

4.1 Atomic force microscopy

In the following, the WS_2 nanosheets after heating and heating/irradiation are examined through AFM. Here we focus on m-WS_2 as a compromise between monolayer content and lateral size. First, we attempted to deposit the samples directly from the dispersion that was heat-treated/irradiated. However, in this case, a lot of non-nanosheet contamination was observed, as exemplarily shown in Figure S12. These can be degradation products on the one hand or residual surfactant, on the other hand. Note that the samples were fairly dilute for the degradation experiments (optical density of 0.4 at 440 nm) to allow for the *in situ* experiments in the PL spectrometer. As such, the ratio of surfactant to nanosheet is much higher than for the deposition of the initial dispersions so that it is not clear whether the contamination is residual surfactant and/or surfactant.

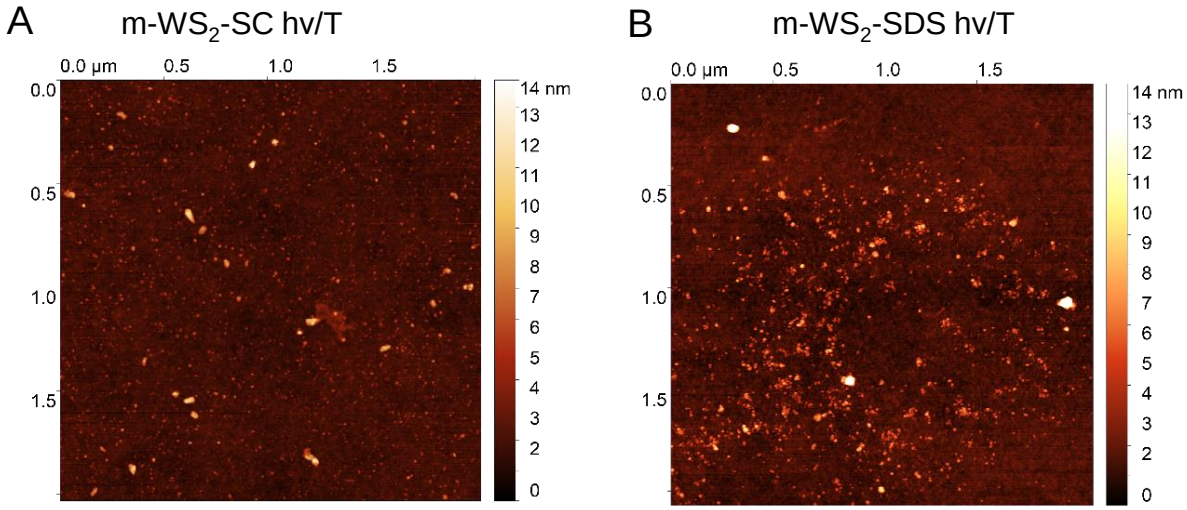

Figure S12: AFM images of m-WS_2 after irradiation/heating to 80°C for 4h. Samples were deposited directly from the dilute dispersion.

Unfortunately, such images would not allow for a characterization of the remaining nanosheets, as it is not clear which deposit is the intact WS_2 after the treatment. Therefore, we performed a centrifugation at 30k *g* (i.e. above the initial upper trapping boundary) and removed water soluble degradation products, as well as surfactant as color-less supernatant and redispersed the sediment in water in ~1/3 of the initial volume. The image quality significantly improved, as shown in Figure S13 for SC and S14 for SDS.

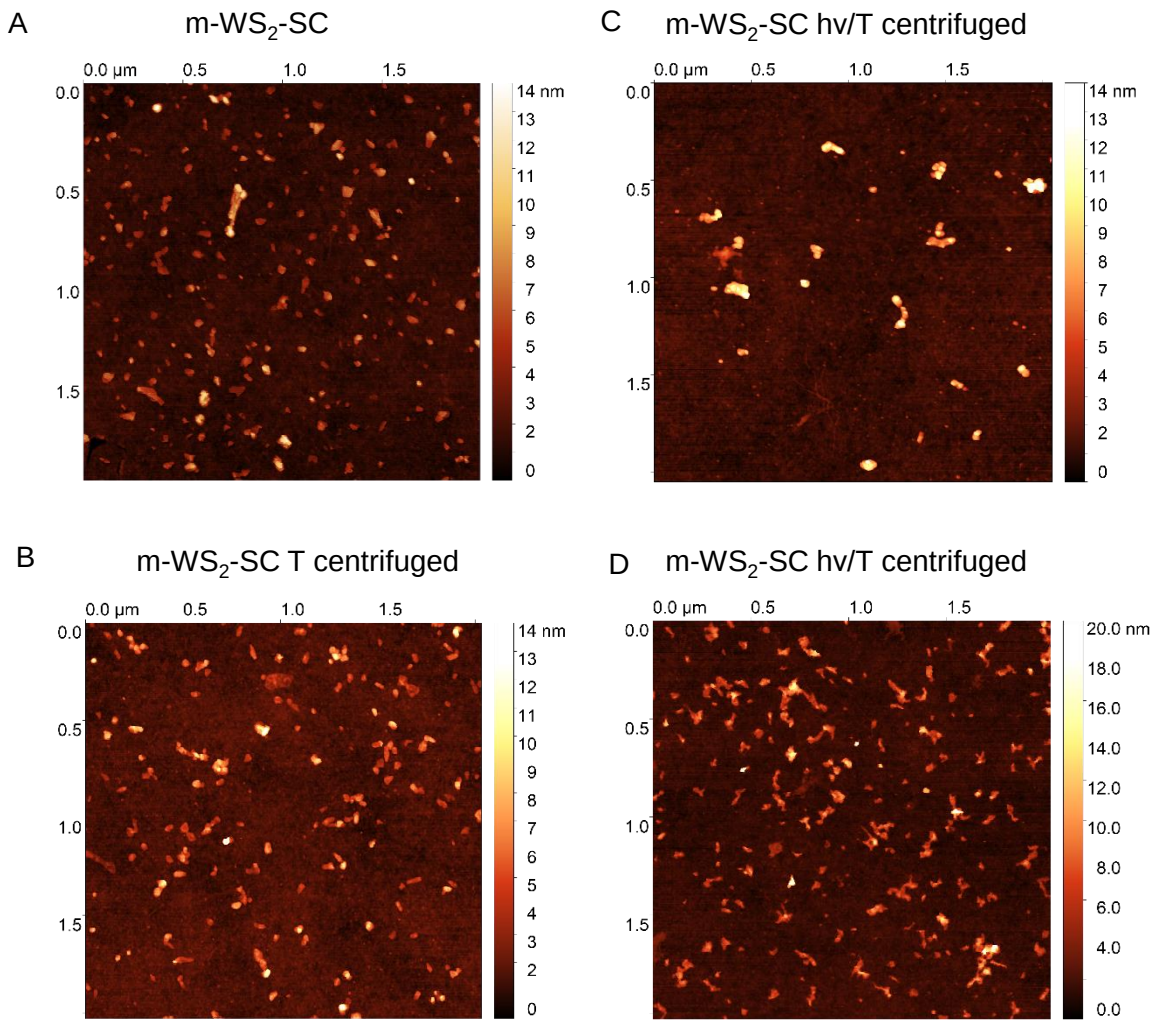

Figure S13: AFM images of m-WS_2-SC after heat treatment and irradiation after purification by centrifugation. A) Initial dispersion of m-WS_2-SC prior to degradation as experiments as reference for direct comparison. B) m-WS_2-SC after heating (80°C, 4h) in the absence of light, C, D) m-WS_2-SC after heating (80°C, 4h) in the presence of light (440 nm) at low coverage (C) and high coverage (D):

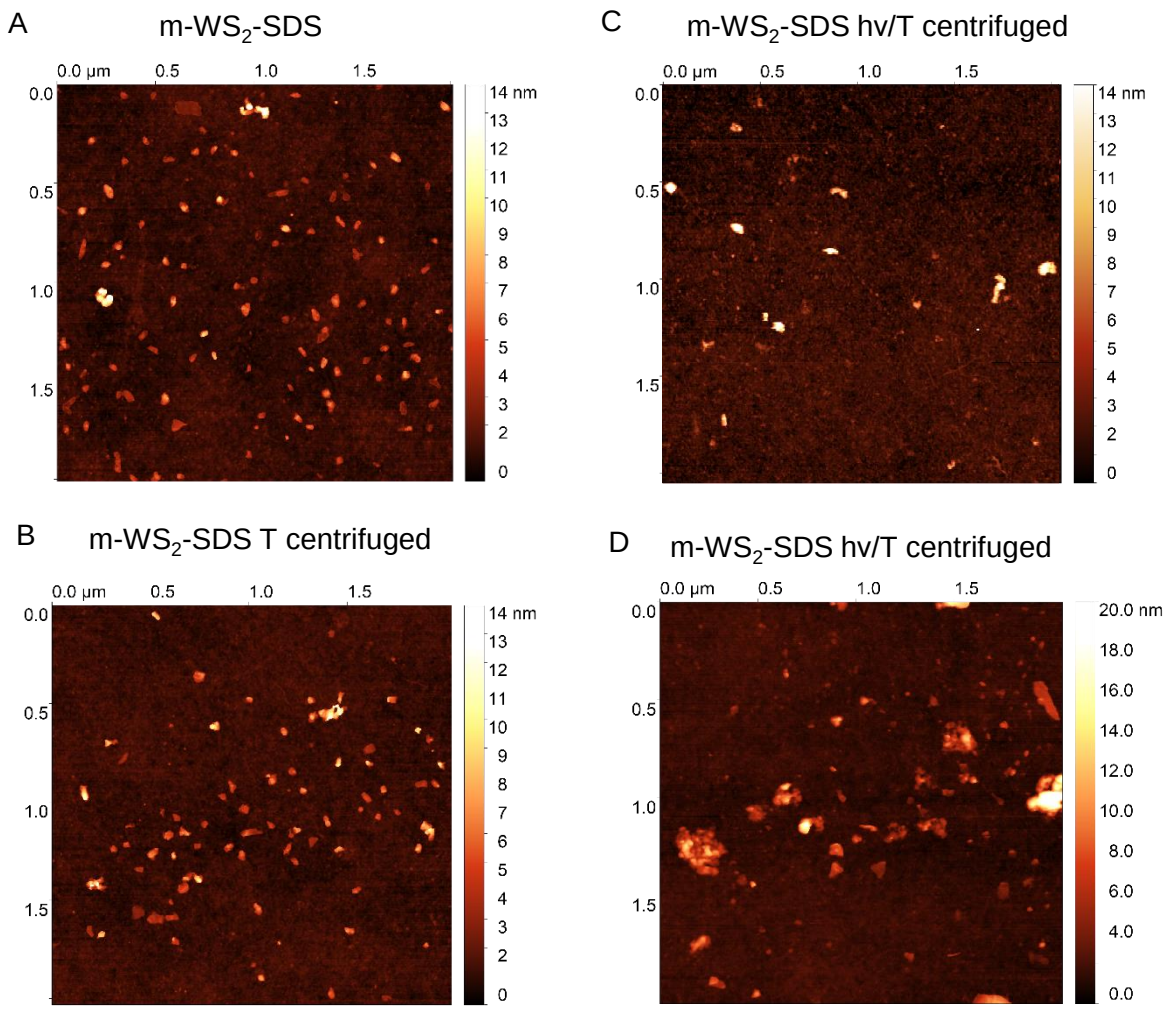

Figure S14: AFM images of m-WS_2-SDS after heat treatment and irradiation after purification by centrifugation. A) Initial dispersion of m-WS_2-SDS prior to degradation as experiments as reference for direct comparison. B) m-WS_2-SDS after heating (80°C, 4h) in the absence of light, C, D) m-WS_2-SDS after heating (80°C, 4h) in the presence of light (440 nm) at low coverage (C) and high coverage (D):

In both SC and SDS, the nanosheets after heating in the absence of light (Figure S13B and S14B) have a similar morphology as in the reference and appear widely intact. After heating and irradiation (Figure S13C,D and S14C,D), the edges are less well defined in most cases. In addition, some aggregation is observed in regions of higher coverage (Figure S13D and S14D) which seems to occur predominantly at edges in the case of SC, while aggregation on the basal plane can be observed in SDS.

To analyze the morphology in more detail, the lateral dimensions and thickness of ~150 individual nanosheets in each sample was measured. The resultant data is shown as histograms in Figures S15 and S16 and as length-thickness scatter plot in Figure S17.

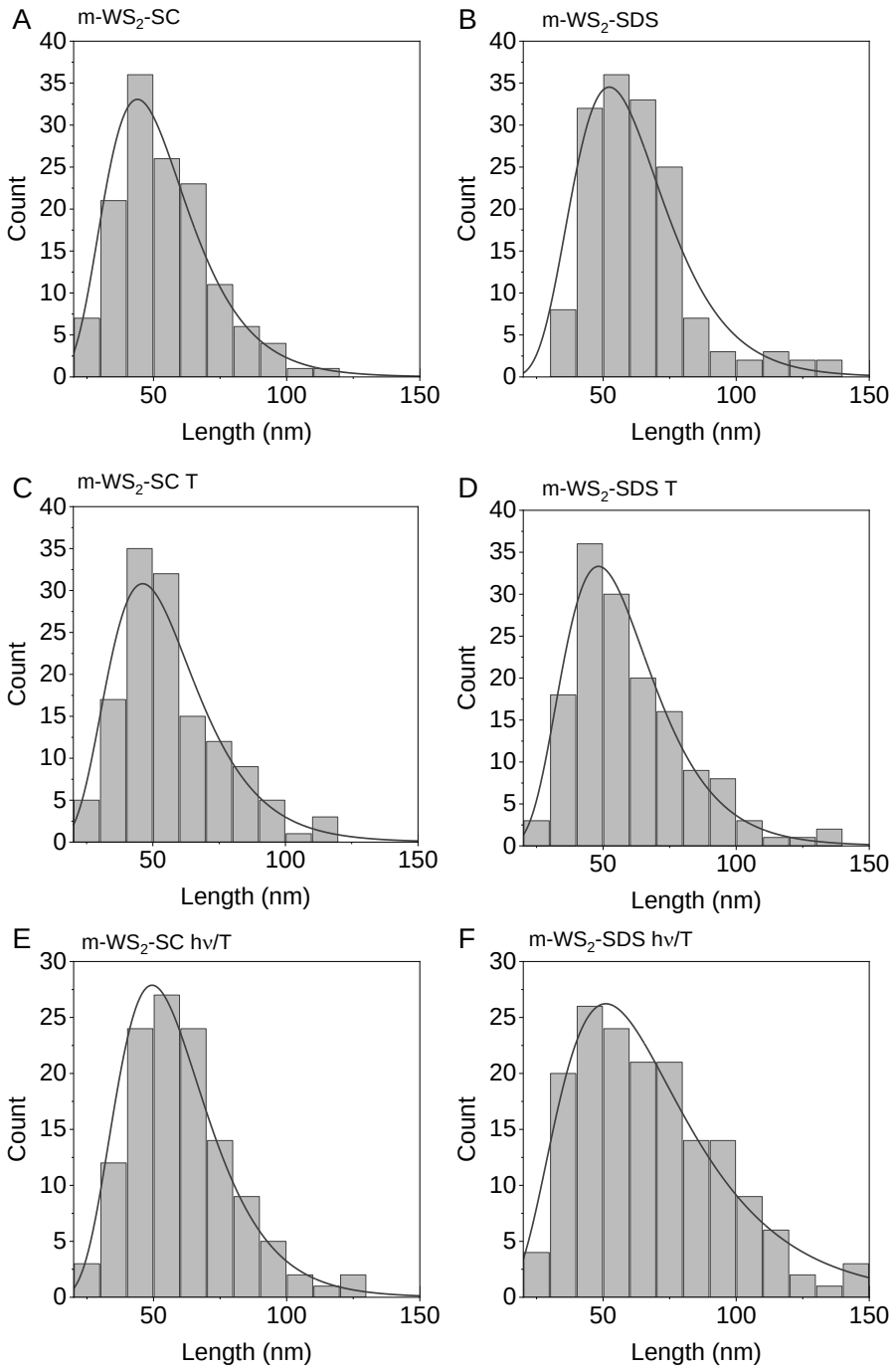

Figure S15: Statistical AFM analysis of the nanosheet length of m-WS_2 after heat treatment and irradiation. A,B) Reference sample prior to degradation in SC (A) and SDS (B). C,D) Samples after heating (80°C, 4h) in the absence of light in SC (C) and SDS (D). E,F) Samples after heating (80°C, 4h) in the presence of light (440 nm) in SC (E) and SDS (F).

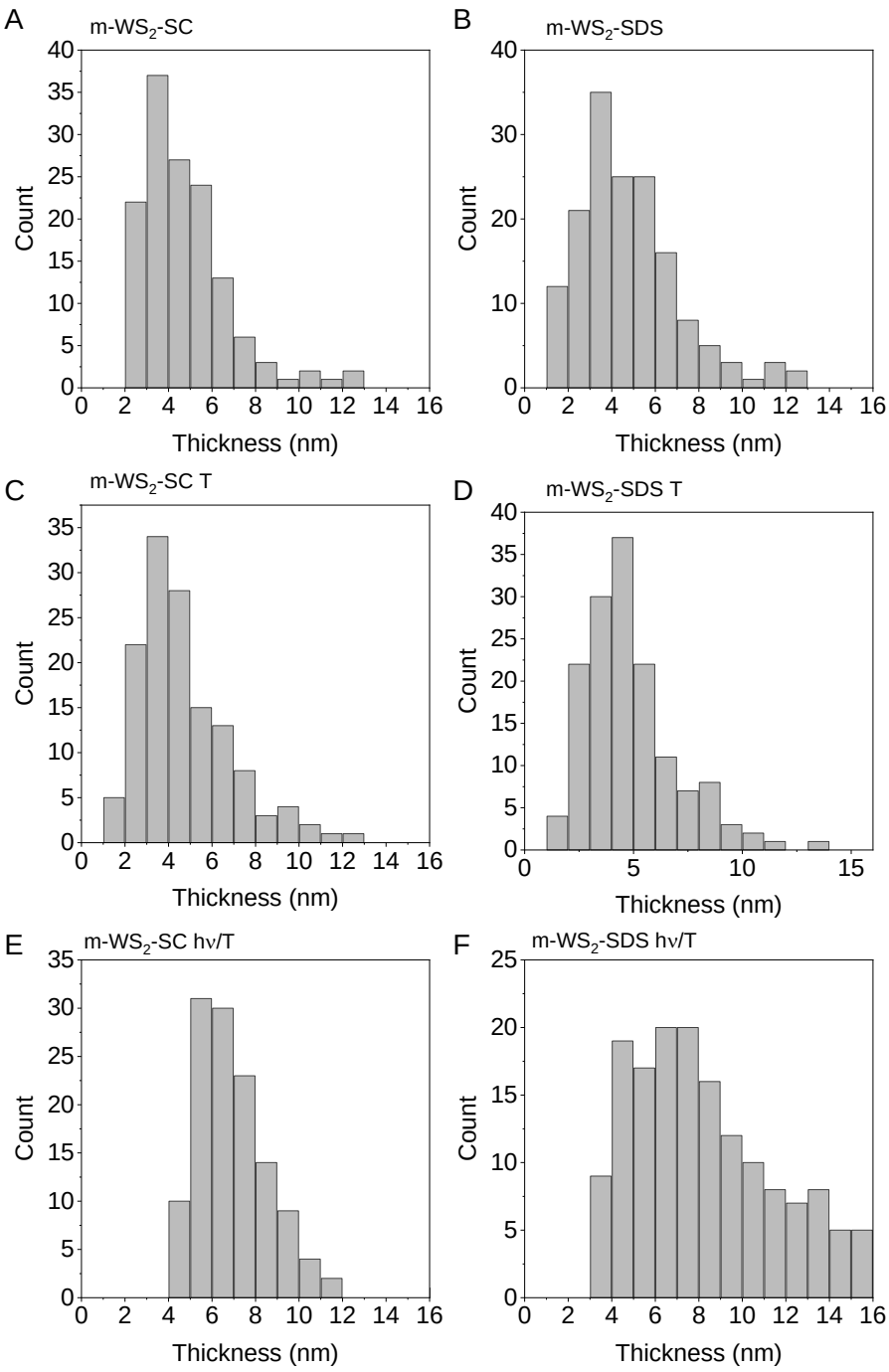

Figure S16: Statistical AFM analysis of the nanosheet thickness of m-WS_2 after heat treatment and irradiation. A,B) Reference sample prior to degradation in SC (A) and SDS (B). C,D) Samples after heating (80°C, 4h) in the absence of light in SC (C) and SDS (D). E,F) Samples after heating (80°C, 4h) in the presence of light (440 nm) in SC (E) and SDS (F).

After heating in the absence of light, neither a change in average length nor thickness is observed in the case of SC (Figures S15B and S16B). This is in agreement with the optical data shown in the main manuscript which suggests that WS_2 is thermally stable when SC is used as surfactant. However, we note that also nanosheets with an apparent thickness < 2.5 nm are now observed in SC. This would be in line with surfactant desorption at elevated temperatures. In the case of SDS, the overall length and thickness distributions are similar (Figures S15D and S16D). However, there is a lower population of the thinnest sheets. This is an agreement with degradation of some of the monolayers that accounts for the reduced PL after heating in SDS.

After heating and simultaneous irradiation, the length distribution remains unchanged in the case of SC (Figure S15E), however it is broadened and extends to larger sheets in the case of SDS (Figure S15F). The thickness histograms clearly show that the thinnest nanosheets are no longer present both in the case of SC and SDS (Figures S16E and S16F). In the case of SC, the population of the few layer sheets remains unaltered which is consistent with a selective degradation of monolayers as already concluded from the A-exciton fine structure of the extinction spectra in the main manuscript. In contrast, in SDS, much thicker sheets are observed. While it appears puzzling that both the length and thickness distribution are broadened and extend to larger/thicker sheets after heating/irradiation in SDS, this can be rationalized through a degradation of monolayers and some of the few-layers in this case (as suggested by the extinction spectra). This is because the lognormal size distribution can have a long tail which can only be resolved after significantly more extensive statistics including more counts. That the distribution histogram approaches 0 for L> 150 nm and N>15 in this sample, does therefore not mean that no larger/thicker sheets are present. However, these will be a minority population. After heating/irradiation, these can be observed due to a destruction of the small/thin sheets.

The above discussion is also clearly reflected in the scatter plots of length as function of thickness in Figure S17. These plots allow for a direct comparison across samples and thus visualize the findings more clearly. Overall, the AFM analysis confirms the degradation of WS_2 monolayer in both SC and SDS through heating and irradiation. This is selective to monolayers in the case of SC, while degradation of few-layers is observed in SDS to some extent. In addition, the data confirms that nanosheets do not degrade by heating in the absence of light in the case of SC, while some destruction of monolayers is observed in SDS.

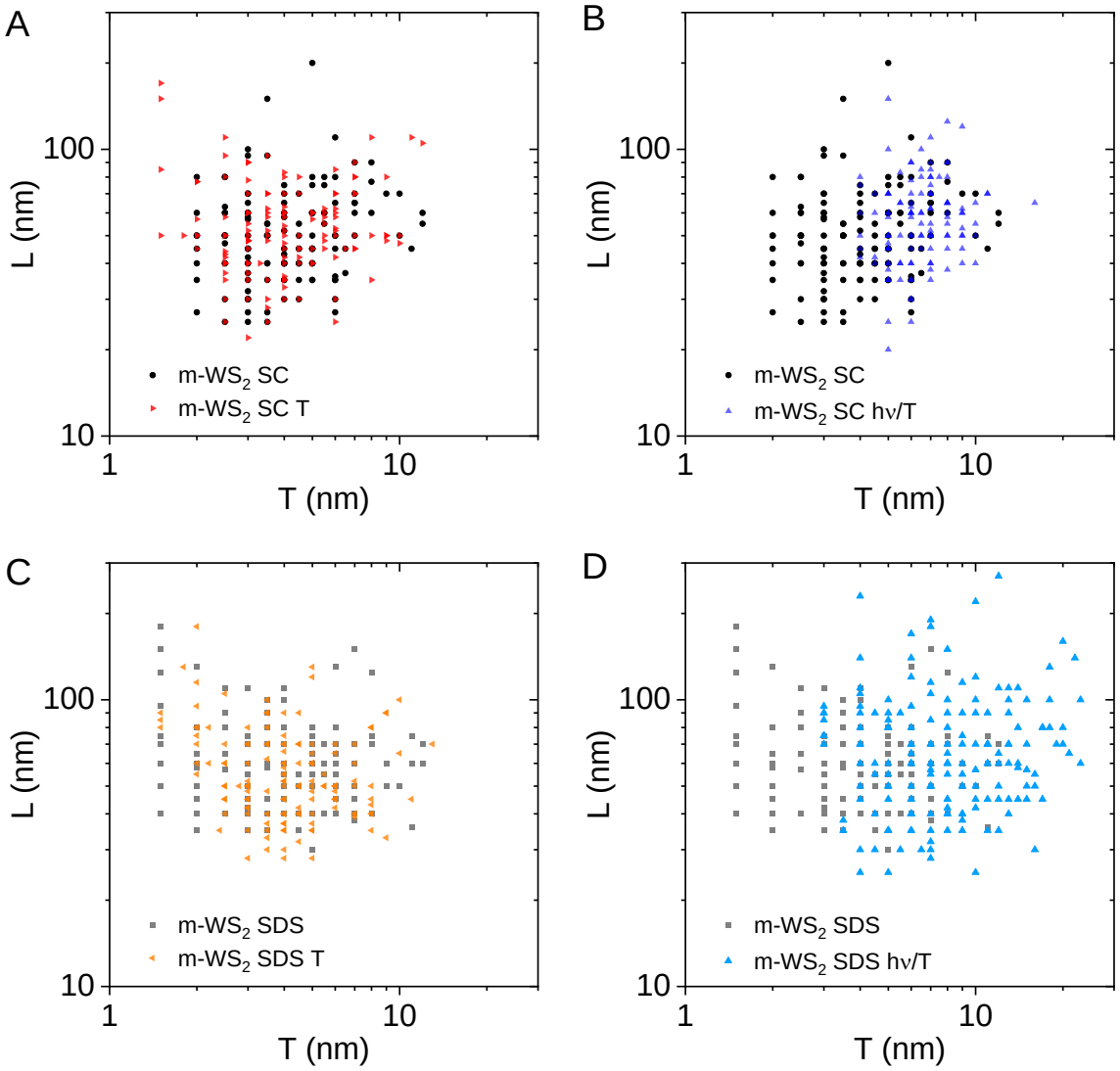

Figure S17: Scatter plots of AFM length as function of thickness of m-WS_2-SC and m-WS_2-SDS after heating (80°C, 4h) and heating/irradiation (80°C, 440 nm, 4h). A, B) m-WS_2-SC. C,D) m-WS_2-SDS. A,C) After heating in the absence of light compared to the same samples prior to heating. B,D) After heating/irradiation in the presence of light compared to the same samples prior to heating

4.2 XPS of WS_2-SC pre and post heating/irradiation

In an attempt to determine the composition of the degradation product, the sample s-WS_2-SC after heating/irradiation to 80°C was first filtered on alumina membranes and subjected to XPS. No sign of oxidation is observed in the core level spectra (Figure S18). This suggests that the degradation products are likely tungstates (W(+VI) oxides) and sulfates (S(+VI) oxides) which are water soluble and removed by filtration.[10] This confirms that nanosheets only partially degrade and that the remaining sheets (which were characterized through AFM above) are widely oxide-free.

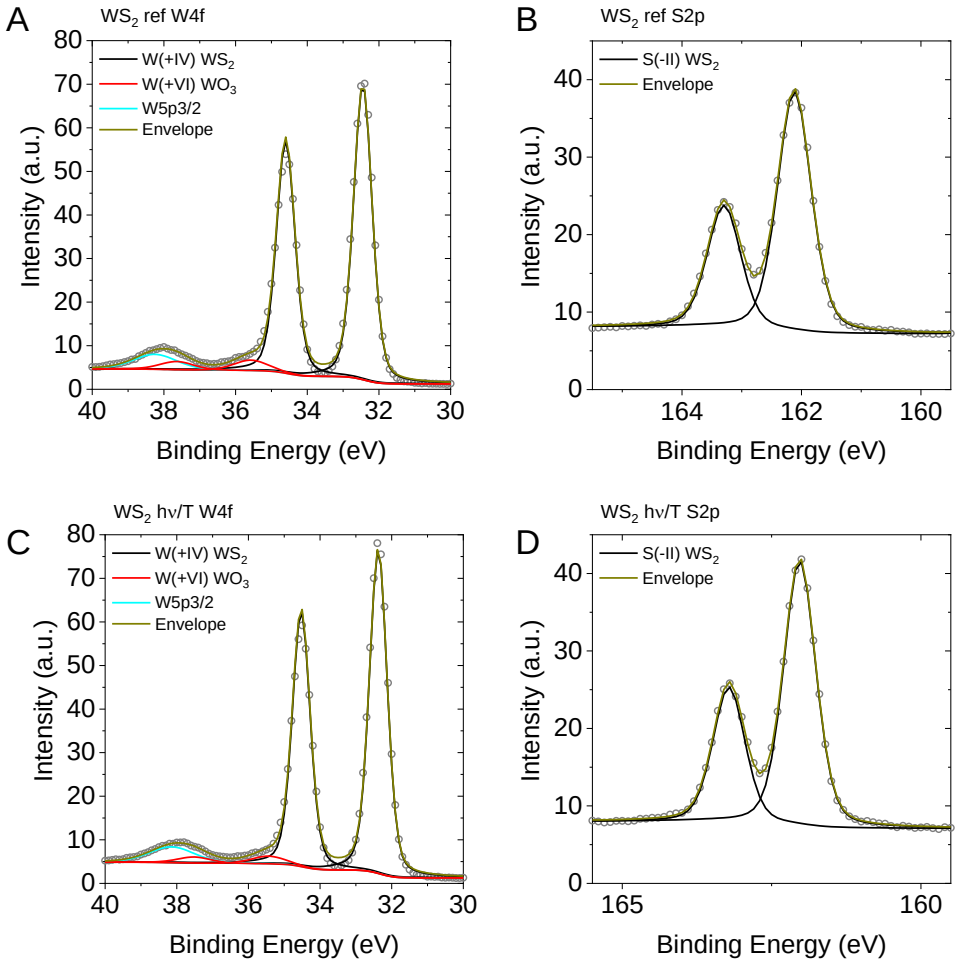

Figure S18: X-ray photoemission spectroscopy of s-WS_2-SC filtered on alumina membranes before (A-B) and after heat treatment/irradiation (C-D). A, C) Fitted W4f core level spectra. B,D) Fitted S2p core level spectra. Fit components are assigned in the figure legend and summarized in Table S2. Only minor signs of W(VI) oxides are observed in both cases. We attribute this to the

production of water soluble degradation products (tungstates and sulfates) which are removed during filtration.

Table S2: Summary of the XPS core level fitting of the s-WS_2-SC reference and heated/irradiated s-WS_2-SC after filtration. Binding energy (BE) and at% of the respective species are given.

	s-WS_2 ref	**s-WS_2 hv/T filtered**
W4f core level		
7/2 W(+IV) WS_2 BE (eV)	32.4	32.4
W(+IV) WS_2 at%	7.5	8.1
7/2 W(+VI) WO_3 BE (eV)	35.6	35.4
W(+VI) WO_3 at%	0.5	0.3
S2p core level		
3/2 S(-II) WS_2 BE (eV)	162.1	162.0
S(-II) WS_2 at%	18.6	20.3

Due to the absence of oxides after filtration, XPS was performed on the reaction mixtures after drop-casting on ITO. Note that these samples will also contain a significant amount of the surfactant and due to the low concentrations that were used for the heating/irradiation experiments, the XPS is challenging with much poorer signal to noise ratio compared to the filtered films. In addition, samples exhibited pronounced charging so that irradiation with a flood gun was performed for charge compensation. The resultant data is shown in Figures S19 (SC) and S20 (SDS). Note that binding energies could not be referenced to adventitious carbon due to the presence of organic molecules.

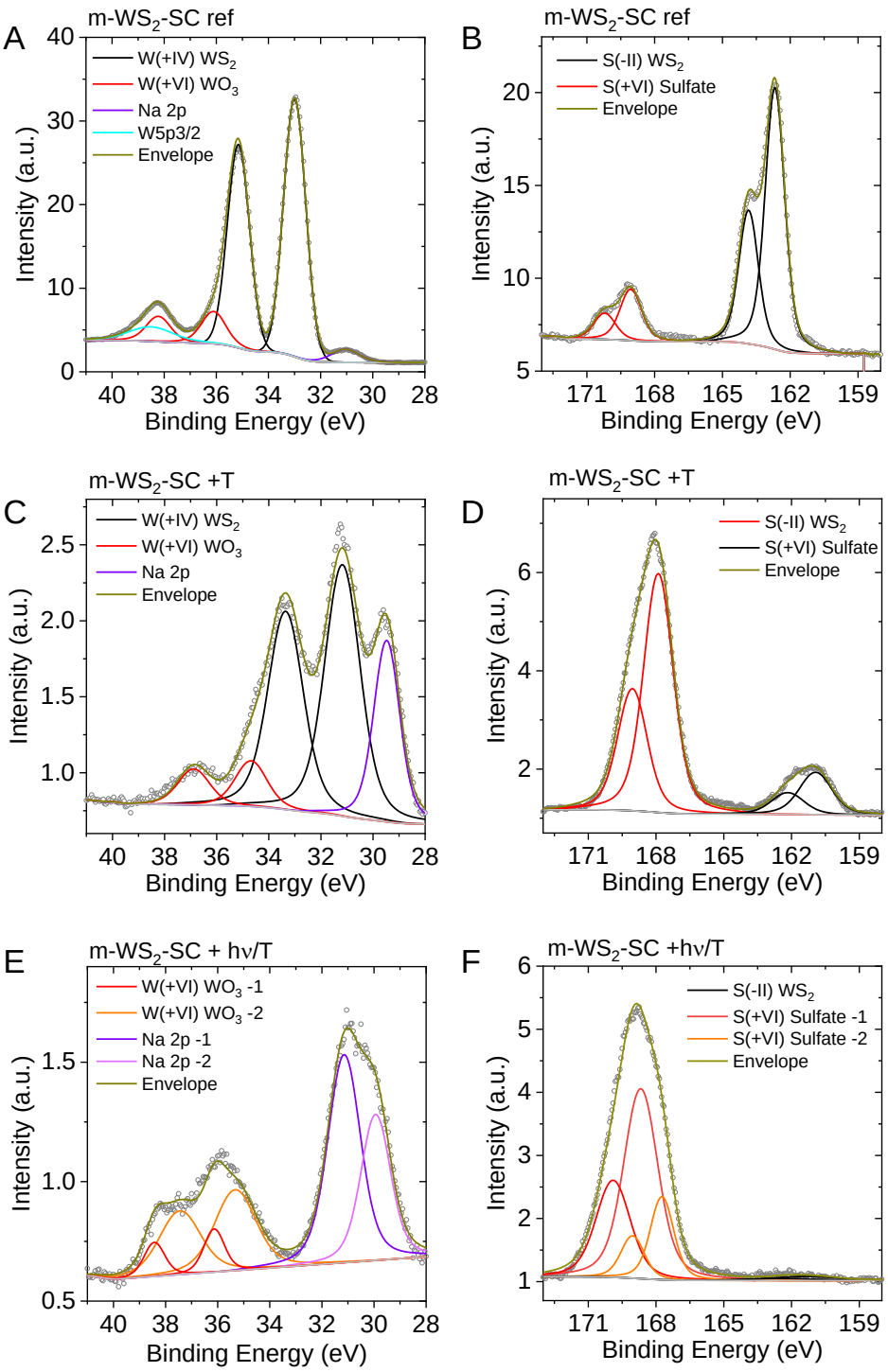

Figure S19: X-ray photoemission spectroscopy of m-WS_2-SC measured on drop-casted samples. A,B) Reference as obtained after LCC. C,D) after heating (4h, 80°C). E,F) and heating/irradiation (4h, 80°C, 440 nm). A, C, E) Fitted W4f core level spectra. B,D,F) Fitted S2p core level spectra. Fit components are assigned in the figure legend and summarized in Table S3.

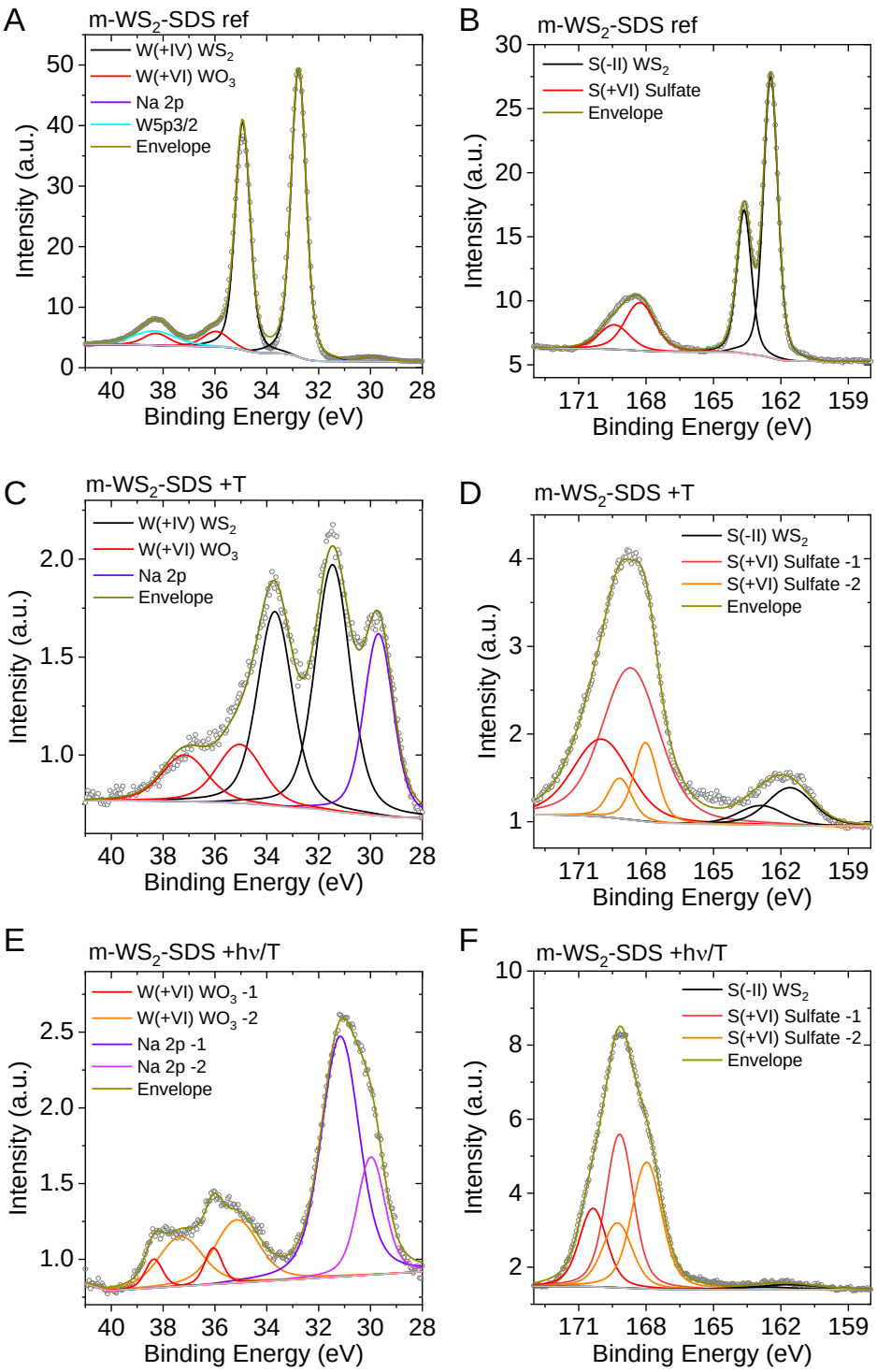

Figure S20: X-ray photoemission spectroscopy of m-WS_2-SDS measured on drop-casted samples. A,B) Reference as obtained after LCC. C,D) after heating (4h, 80°C). E,F) and heating/irradiation (4h, 80°C, 440 nm). A, C, E) Fitted W4f core level spectra. B,D,F) Fitted S2p core level spectra. Fit components are assigned in the figure legend and summarized in Table S3.

Table S3: Summary of the XPS core level fitting of the m-WS_2-SC references, heated and heated/irradiated m-WS_2-SC m-WS_2-SDS after drop-casting the dilute dispersions on ITO. Binding energy (BE) and at% of the respective species are given.

	m-WS_2 SC	**m-WS_2-SC + T**	**m-WS_2-SC + hν/T**	**m-WS_2 SDS**	**m-WS_2-SDS + T**	**m-WS_2-SDS + hν/T**
W4f core level						
7/2 W(+IV) WS_2 BE (eV)	33.0	31.2		32.7	31.5	
W(+IV) WS_2 at%	3.8	0.33		4.94	0.26	
7/2 W(+VI) WO_3 – 1 BE (eV)	36.1	34.7	35.4	36.0	35.0	35.2
W(+VI) WO_3 – 1 at%	0.58	0.05	0.11	0.45	0.08	0.09
7/2 W(+VI) WO_3 – 2 BE (eV)			37.4			36.1
W(+VI) WO_3 – 2 at%			< 0.01			0.02
S2p core level						
3/2 S(-II) WS_2 BE (eV)	162.7	160.9	161.4	162.5	161.6	161.6
S(-II) WS_2 at%	10.0	0.91	0.19	12.9	0.67	0.23
3/2 S(+VI) Sulfate BE (eV) Surfactant/contamination	169.1	167.9	168.7	168.3	168.7	169.2
(+VI) Sulfate at% Surfactant/contamination	2.2	4.7	1.79	4.65	3.40	3.42
3/2 S(+VI) Sulfate BE (eV) Degradation product			167.7		168.0	168.0
(+VI) Sulfate at% Degradation product			1.36		0.73	3.07

Table S4: Ratio of sulphur to tungsten signal from XPS calculated from fitting respective core level spectra. Strong deviations from the expected 2:1 ratio are observed in the drop-casted samples due to sulfate in the surfactant and/or as potential contamination. The increase in the S/W ratio in the drop-cast *versus* the filtered WS_2-SC reference suggests that the sulfate observed in this case is at least partially due to sulfate contaminations in the surfactant solution rather than oxidation associated with WS_2.

Sample	**S/W ratio**
Filtered	
s-WS_2-SC reference	2.3
s-WS_2-SC +hν/T	2.4
Drop-cast	
m-WS_2-SC reference	2.8
m-WS_2-SC +T	14.7
m-WS_2-SC +hν/T	43.6
m-WS_2-SDS reference	3.3

m-WS_2-SDS +T	14.0
m-WS_2-SDS+hν/T	61.1

4.3 Raman spectroscopy

Raman spectroscopy was performed on the same samples subjected to XPS after drop-casting on ITO. In the as-recorded spectra with 532 nm excitation over a wide-spectral range (Figure S21B,C), a background is observed in addition to the WS_2 Raman modes. This can at least be partially attributed to the ITO glass substrate (Figure S21A). In the case of the initial dispersion prior to heat treatment, this background is minor since a higher concentration of WS_2 was used for deposited resulting in a thicker film. In this case, some photoluminescence of WS_2 is observed (black trace in Figure S21B,C), albeit weaker and broadened compared to the measurement in dispersion (compare to Figure S1). This is due to restacking of the sheets on deposition. After heating in the absence of light (red trace in Figure S21B,C), this PL is still observed to some extent, but superimposed on the ITO glass background due to lower coverage. The spectra after heating/irradiation show a further increased background (blue trace in Figure S21B,C). While it cannot be excluded that this partially stems from trion emission or degradation products, we note that this was not observed for the measurements in dispersion in the PL spectrometer with 440 nm excitation (example see Figure S22). We therefore believe it is not attributed to trion emission from WS_2.

To analyze the Raman modes after excitation with 532 nm and 633 nm, the spectra in the range of 100-750 cm^{-1} were baseline corrected and normalized to the most intense WS_2 Raman mode (Figure S23). Even though oxidation after heating/irradiation is clearly evident from XPS, no change in the Raman modes are observed. We attribute this to the orders of magnitude enhanced Raman signal of resonantly excited WS_2 opposed to degradation products.

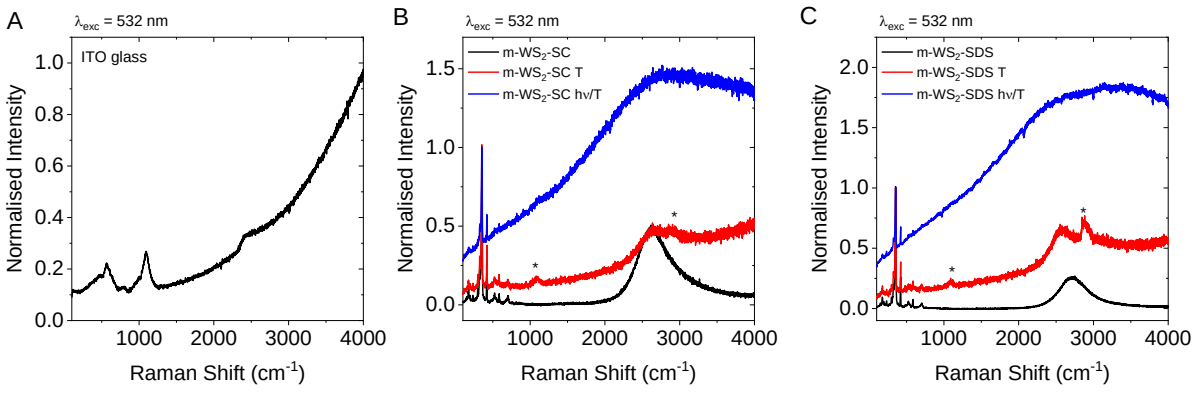

Figure S21: Raman spectra of m-WS_2 after heating and heating/irradiation over a wide spectral region on dispersions drop-cast on ITO glass with an excitation wavelength of 532 nm. A) Spectrum of the ITO glass. B) m-WS_2 SC, C) m-WS_2-SDS. The WS_2 Raman spectra were normalized to the 2LA(M) Raman mode without any baseline subtraction.

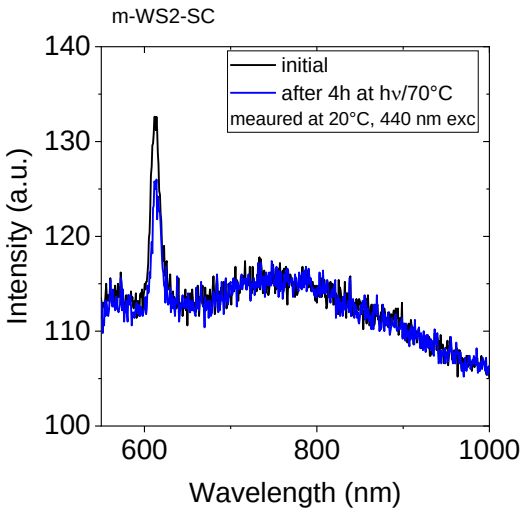

Figure S22: Example of a PL spectrum after heating/irradiation measured in the fluorescence spectrometer in dispersion with an excitation wavelength of 440 nm. No increased background is observed.

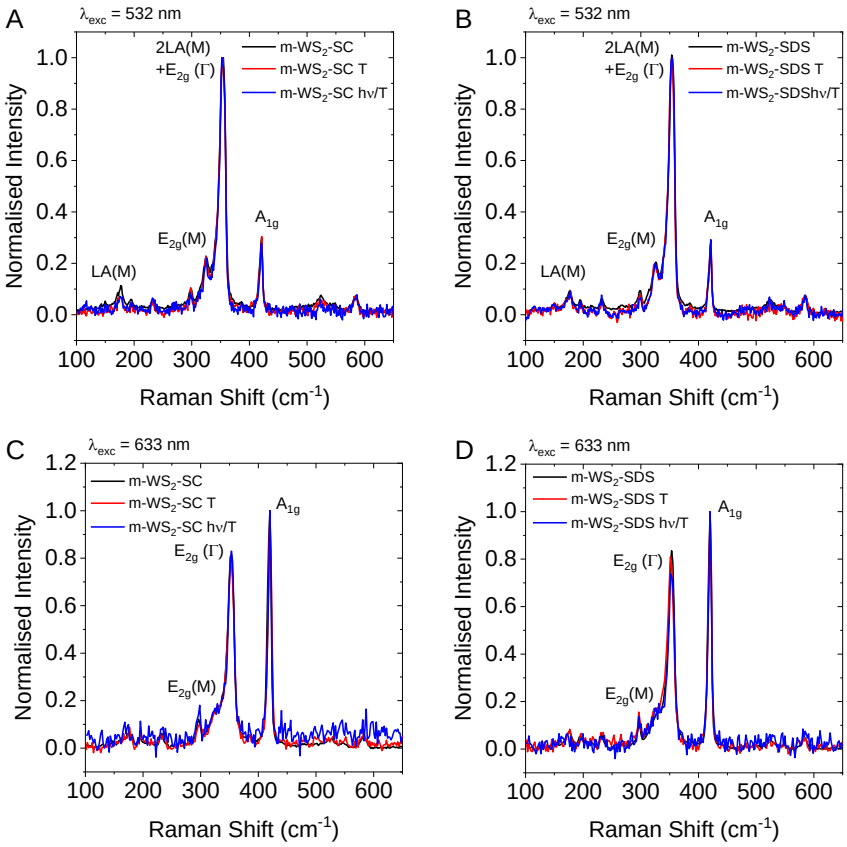

Figure S23: Baseline-corrected and normalized Raman spectra of m-WS_2 after heating and heating/irradiation after drop-casting on ITO glass. A,B) Excitation wavelength 532 nm, C,D) Excitation wavelength 633 nm. A,C) m-WS_2-SC and B,D) m-WS_2-SC.

5. Detailed analysis of degradation kinetics in SDS

5.1 Deconvoluting thermal and photoinduced decay

All decay kinetics of WS_2-SDS shown in Figure S10 were deconvoluted into fast and slow reactions, as is outlined in the main manuscript. Then exponential fits were applied to slow and fast reactions alike, as both follow first order kinetics. The results obtained for the lifetimes of slow (thermal) and fast reaction (photo-induced) pathways are depicted in Figure S24.

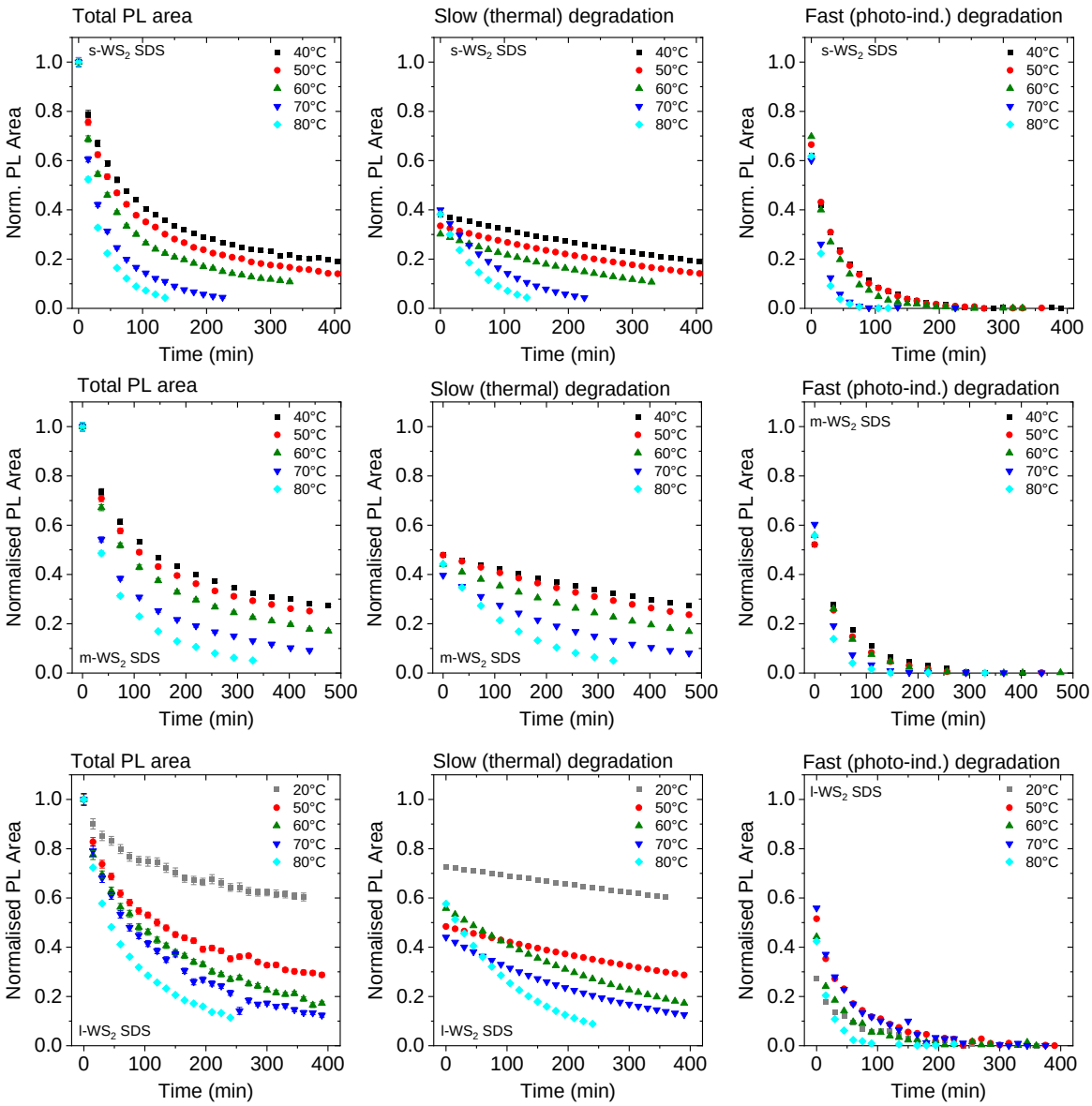

Figure S24: Deconvolution of the degradation kinetics of size-selected WS_2-SDS into thermal and photo-induced degradation. Top: s-WS_2, middle: m-WS_2, bottom: l-WS_2. Left: Total PL area measured as function of time normalized to the PL area of the first measurement prior to heating. Middle: Slow (thermal) decay. The last 4-8 data points of the measured total PL was fit to a linear

regression on the semi-logarithmic scale and the function extrapolated to shorter times. Right: Fast (photo-induced) decay obtained from subtracting the data of the slow decay from the total PL area measured.

Linear behaviour in an Arrhenius plot was found for both reaction speeds and all sizes (Figure S25), albeit with some scatter. As before, in particular, the dataset of the large nanosheets shows significant scatter. The reason is probably lower overall PL emission from this fraction due to the lower monolayer content, which results in worse spectral quality which increases the uncertainty in the overall fitting and data treatment. The activation energies of the large fraction thus have to be treated with care. Nonetheless, the obtained E_As show no size dependence- neither for the thermal nor the photochemical reaction.

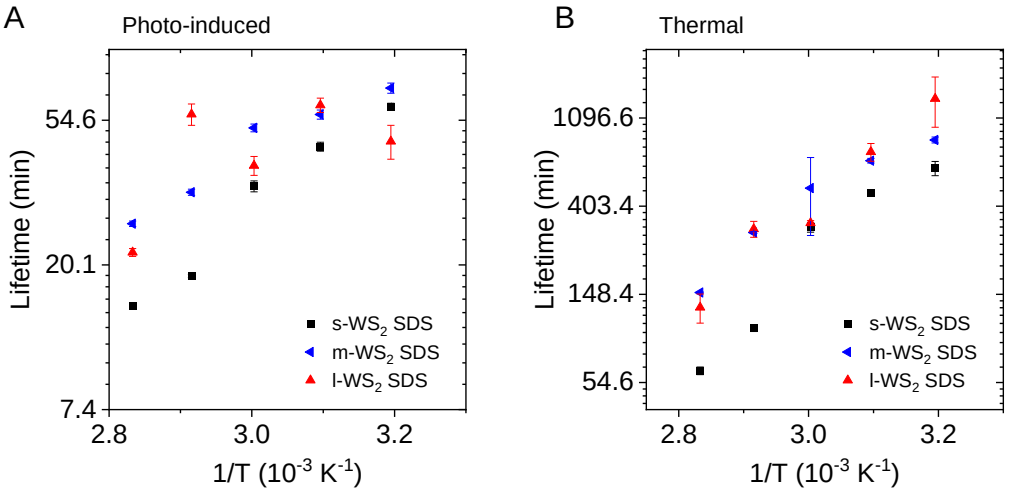

Figure S25: Arrhenius-type plot of the decay of size-selected WS_2-SDS. Lifetimes of the decays in Figure S24 as function of inverse temperature on a semi-logarithmic scale. A) Fast, photo-induced decay, B) Slow, thermal decay. While there is some scatter in the data, it is clear that no pronounced size dependence of the degradation is observed.

5.2 Portion of reacted material and mechanistic considerations

In this section, the relative product formation will be discussed in detail leading to some mechanistic considerations.

In the case of the decay of WS_2 in SC, the portion of reacted material can be determined from the single-exponential decays shown in Figure S8 left in analogy to previous work.[11] This is shown for small and large nanosheets in Figure S26A. Consistent with AFM (SI section 4), the monolayered nanosheets almost completely degrade even at 40°C in the case of s-WS_2, while some PL of large nanosheets is retained even after heating and irradiation to 80°C. No clear trend with temperature is observed.

For the SDS data sets, the portion of unreacted material p_∞ can be extracted from the biexponential fit (equation 1 in the main manuscript; fits see Figure S10, left), using the fit results for $[A_{constant}]$,

$$p_\infty = \frac{[A_{constant}]}{A_1+A_2+[A_{constant}]}, \quad (3)$$

With p_∞ being the portion of material that is left after completion giving the portion that reacted material in total as $1-p_\infty$. The resultant data is shown in Figure S26B. The portion of reacted material increases with increasing temperature reaching 100% at 80°C for both large and small sheets. At lower temperatures, the monolayers in l-WS_2 degrade less completely.

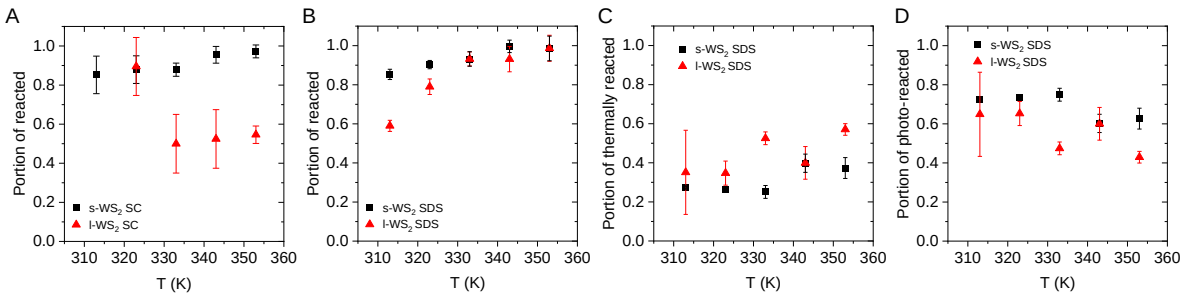

Figure S26 Portion of degraded material. A) Portion of degraded WS_2 in SC extracted from fitting the PL kinetics to a single exponential. B) Portion of degraded WS_2 in SDS extracted from fitting the PL kinetics to a double exponential. C) Portion of thermally degraded WS_2 in SDS and D) photo-chemically degraded WS_2 in SDS as described in the text.

The portion that reacted in total ($1-p_\infty$), can be converted to the portion of material which decayed thermally p_T:

$$p_T = \frac{y_0-p_\infty}{1-p_\infty}, \quad (4)$$

where y_0 is the initial value of the photochemical decay law (which is close to 1 in the normalized data), calculated by extrapolation of the slow degradation pathway *via* the deconvolution method described in the main manuscript. Similarly, equation 4 can be reversed to output $p_{photochemical}$ if y_0, is substituted for the initial amount stated in the photochemical decay law. The results of this data analysis is plotted in Figure S26C-D.

Interestingly, the portion of thermally degraded WS_2 in SDS is larger for l-WS_2 than s-WS_2 (Figure S26C). This appears counterintuitive. However, it is important to recall that only relative populations are extracted this way, *i.e.* the data implies that smaller nanosheets are more prone to photo-induced degradation than larger ones. Overall, this means that the relative rates for photochemical degradation and thermal degradation exhibit a size dependence. The extracted activation energies for these processes however, show no clear size dependence (Table 1 in the main manuscript). The observed difference can be understood with the following geometric considerations.

On the molecular level, the studied reactions are expected to be the same, *i.e.* independent of the respective sheet size. For estimation of the reaction rates we can consider the Arrhenius equation,

$$k = A_{Arrhenius} \cdot e^{\frac{-E_A}{RT}}. \qquad (5)$$

Since the same reaction is investigated on the molecular level, $A_{Arrhenius}$ is assumed to be independent of sheet size.[12] Further, the experimental results show no size dependence for E_A. Therefore, no size dependence on *k* is expected.

Instead of concentrations, which are usually studied in chemical reaction kinetics, here the PL emission is investigated. The PL emission will stem selectively from ML WS_2. As a simplification, here the PL is assumed to be proportional to the ML nanosheet area. Further, the nanosheets are approximated as disks of radius *r* with area *A*, for which two degradation pathways are considered, decay *via* the basal plane or *via* the edge. Both degradation pathways have been proposed for TMDs in the literature[8a] and a schematic of both reactions is shown in Figure S27.

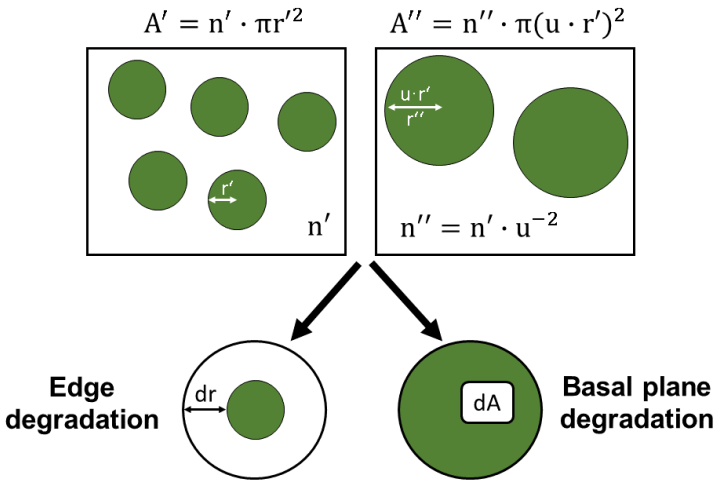

Figure S27: Schematic overview of the reaction model described to rationalize the size dependence of the portion of reacted material for photochemical and thermal degradation pathways.

Two fractions of nanosheets with different sizes and the same total PL can be described by two arrays of disks with different area per disk, but same total area in a volume fraction as is shown in Figure S27 in the top left and top right. The conditions chosen here are as follows, r' is the radius of each disk in array' and r'' = u·r' is the radius of each disk in array''. Each array's total area, *i.e.* the area of all disks in a certain volume fraction combined, will be given by,

$$A_{total} = n \cdot \pi r^2, \qquad (6)$$

with n' and n'' being the number of disks per volume fraction. With the above conditions, there should be u^{-2} times more disks in array' then in array'' to satisfy equal initial areas in a certain volume fraction.

A decay of an increment of basal plane dA, describes direct basal plane oxidation. The total area will then be,

$$A_{total} = A_0 - dA, \qquad (7)$$

with initial total area A_0. Equation 7 leads to the same amount of area reduction and thus PL intensity decrease for both arrays. Therefore, a basal plane centered degradation is not expected to show any size dependence in the framework of this model.

Reaction progression for attack from the nanosheet edge can be envisioned as oxide formation on the sheet's circumference. Upon degradation, the active sheet area will, therefore, be diminished, measured from the edge to the circular sheet's center. This can be described mathematically by an incremental change dr of the radius. Therefore, the area decay for n discs will be given by,

$$A_{total} = n \cdot \pi(r - dr)^2 = n \cdot \pi r^2 - n \cdot 2\pi r dr + n \cdot \pi dr^2, \quad (8)$$

which can be simplified by setting $0 = n \cdot \pi dr^2$, which is reasonable as dr is an incremental change. Furthermore, $n \cdot \pi r^2$ can be replaced by A_0 yielding,

$$A_{total} = A_0 - n \cdot 2\pi r dr. \quad (9)$$

Application of the boundary conditions illustrated in Figure S27 affords,

$$A' = A_0 - n' \cdot 2\pi r' dr \quad (10)$$

and

$$A'' = A_0 - n'' \cdot 2\pi r'' dr = A_0 - n' \cdot u^{-2} \cdot 2\pi r' \cdot u \cdot dr = A_0 - \frac{2\pi r' dr}{u}. \quad (11)$$

Therefore, in this decay law, the radii of the disks will have an influence on the overall degradation speed, as increasing the radius by a factor *u* leads to deceleration of the reaction by this factor. This means that for an edge-centered degradation pathway, the reaction will be slower for larger sheets. What really differs between the two discussed arrays, or for that matter two nanosheet fractions of different size, is the amount of material that can be attacked *via* the edge, which is the total circumference in a certain volume fraction. Note that the assumption of circular sheets has no physical basis, but the qualitative dependence on sheet size will be equally true for any other shape, although not with the same anti-proportionality.

In summary, in our experiments, the portion of photochemically-degraded WS_2 was larger for smaller nanosheet sizes in both SC and SDS. Photochemical degradation therefore seems to speed up relative to the thermal reaction upon sheet size reduction. Within the framework of the model elaborated here, this result can be explained with a preferentially edge centered photochemical degradation and basal plane centered thermal decay. This does not mean however that the photochemical degradation exclusively takes place on the edge, as only relative weights are accessible. The thermal reaction pathway is supressed in SC as surfactant which can be applied by shielding of the basal plane with the facial amphiphile as previously suggested.[6]

6. WS_2-SC-cys

6.1 Degradation followed by photoluminescence and extinction

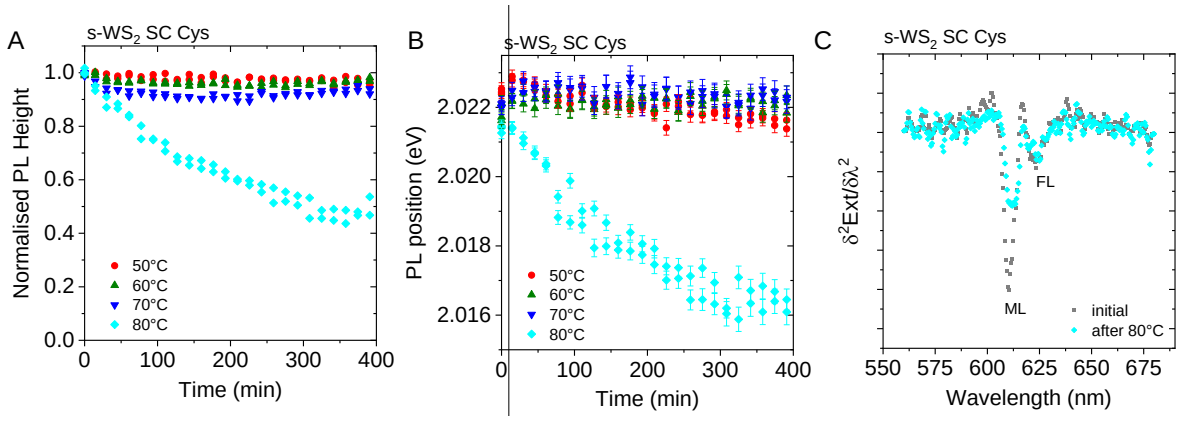

Figure S28: Additional data on the degradation of s-WS_2-SC-cys. A) Normalized PL height and B) PL position as function of time after heating/irradiation at different temperatures. C) Second derivative of the A-exciton extinction of the initial dispersion and after heating/irradiation to 80°C for 400 min.

6.2 Dilution of a WS_2-SC dispersion with cysteine

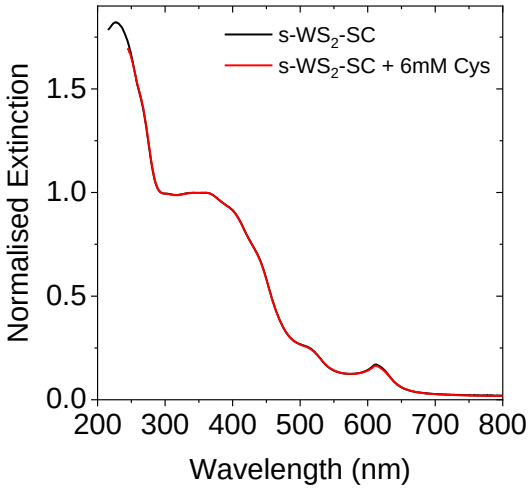

Figure S29: Extinction spectra of s-WS_2-SC after dilution with cysteine compared to the initial dispersion**.** In contrast to exfoliation in the presence of cysteine, no additional peaks in the UV region are observed.

6.3 XPS

In contrast to the drop-casted samples after heating and irradiation, concentrated dispersions after LCC were deposited to minimize the additional contributions from surfactant. No apparent charging was observed and hence no charge compensation with a flood gun was performed. Note that binding energies could not be referenced to adventitious carbon due to the presence of organic molecules.

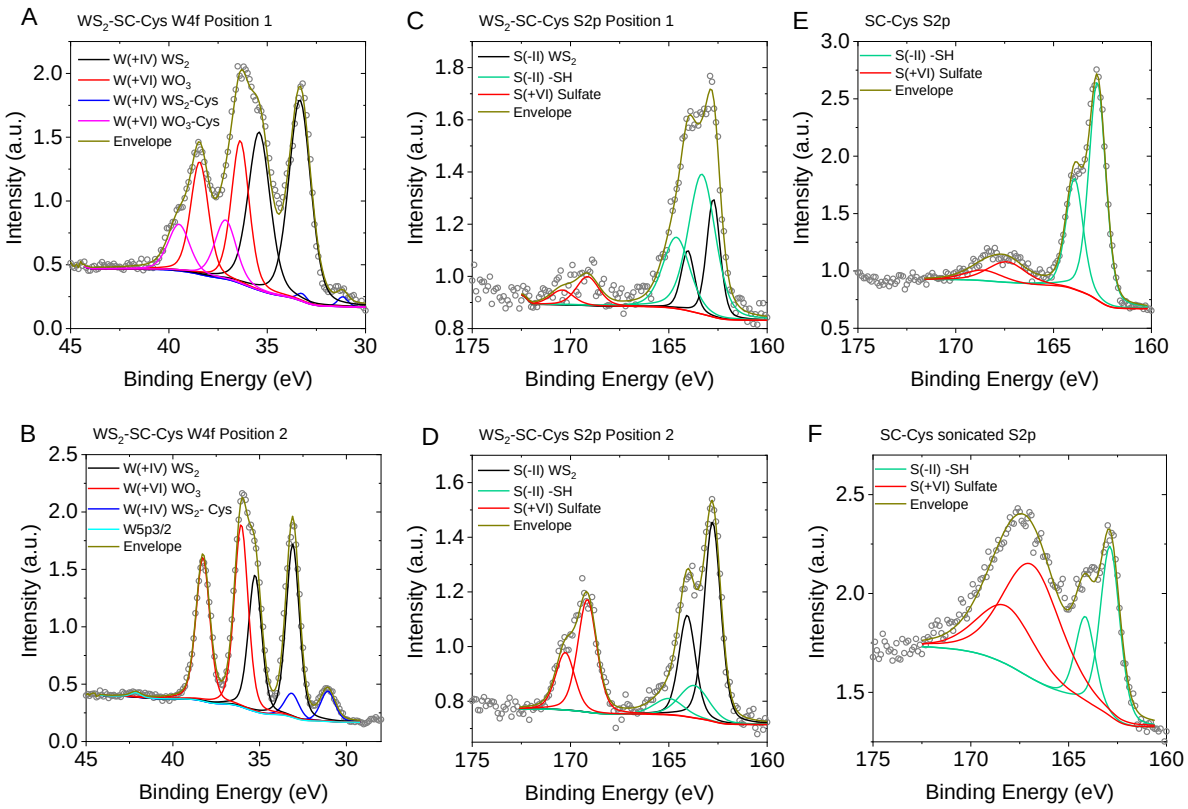

Figure S30: Fitted XPS core level spectra of WS_2-SC-cys measured in different sample regions compared to S2p core level spectra of pure and sonicated cysteine. A-B) W4f core level spectra of WS_2-SC-cys in sample area 1 (A) and 2 (B). C-D) S2p core level spectra of WS_2-SC-cys in sample area 1 (C) and 2 (D). E) S2p core level spectrum of SC-cysteine sample drop-cast on Si/SiO_2. F) S2p core level spectrum of a sonicated SC-cysteine solution in water drop-cast on Si/SiO_2. Results of the data fitting are summarized in table S5.

Table S5: Summary of the XPS core level fitting of the s-WS_2-SC reference drop-cast WS_2-SC-cys measured at two positions, cysteine solution drop-cast on Si/SiO_2 before and after sonication. Binding energy (BE) and at% of the respective species are given.

	s-WS_2 ref filtered	**s-WS_2-cys 1**	**s-WS_2-cys 2**	**Cys-SC**	**Cys-SC son**
W4f core level					
7/2 W(+IV) WS_2 BE (eV)	32.4	33.1	33.1		
W(+IV) WS_2 at%	7.5	10.4	13.4		
7/2 W(+VI) WO_3 BE (eV)	35.6	36.4	36.1		
W(+VI) WO_3 at%	0.5	13.3	14.6		
7/2 W(+IV) WS_2-Cys BE (eV)		31.3	31.1		
W(+IV) WS_2-Cys at%		0.8	2.5		
7/2 W(+VI) WO_3-Cys BE (eV)		37.3			
W(+VI) WO_3-Cys at%		4.5			
S2p core level					
3/2 S(-II) WS_2 BE (eV)	162.1	162.7	162.8		
S(-II) WS_2 at%	18.6	18.9	35.8		
3/2 S(-II) -SH BE (eV)		163.3	163.7	162.8	162.9
S(-II) -SH at%		44.3	10.3	6.2	3.2
3/2 S(+VI) Sulfate BE (eV)		169.1	169.2	167.4	166.9
(+VI) Sulfate at%		7.8	23.3	1.3	6.0
C1s core level					
BE (eV)	286.6	285.5	285.4	284.3	284.5
at%	37.7	72.1	70.2	15.1	18.1
N1s core level					
BE (eV)	407.4	401.1	400.5	400.3	400.5
at%	4.1	0.8	0.6	6.7	2.4

References

[1] a) C. Backes, B. M. Szydłowska, A. Harvey, S. Yuan, V. Vega-Mayoral, B. R. Davies, P.-l. Zhao, D. Hanlon, E. J. G. Santos, M. I. Katsnelson, W. J. Blau, C. Gadermaier, J. N. Coleman, *ACS Nano* **2016**, *10* 1589-1601; b)K. Synnatschke, P. A. Cieslik, A. Harvey, A. Castellanos-Gomez, T. Tian, C.-J. Shih, A. Chernikov, E. J. G. Santos, J. N. Coleman, C. Backes, *Chem. Mater.* **2019**, *31*, 10049-10062.

[2] C. Backes, B. M. Szydłowska, A. Harvey, S. Yuan, V. Vega-Mayoral, B. R. Davies, P.-l. Zhao, D. Hanlon, E. J. G. Santos, M. I. Katsnelson, W. J. Blau, C. Gadermaier, J. N. Coleman, *ACS Nano* **2016**, *10*, 1589-1601.

[3] Y. Niu, S. Gonzalez-Abad, R. Frisenda, P. Marauhn, M. Drüppel, P. Gant, R. Schmidt, N. Taghavi, D. Barcons, A. Molina-Mendoza, S. de Vasconcellos, R. Bratschitsch, D. Perez De Lara, M. Rohlfing, A. Castellanos-Gomez, *Nanomater.* **2018**, *8*, 725.

[4] a) L. Ueberricke, J. N. Coleman, C. Backes, *Phys. Status Solidi B* **2017**, *254*, 1700443; b) C. Backes, D. Campi, B. M. Szydlowska, K. Synnatschke, E. Ojala, F. Rashvand, A. Harvey, A. Griffin, Z. Sofer, N. Marzari, J. N. Coleman, D. D. O'Regan, *ACS Nano* **2019**, *13*, 7050-7061.

[5] C. Backes, R. J. Smith, N. McEvoy, N. C. Berner, D. McCloskey, H. C. Nerl, A. O'Neill, P. J. King, T. Higgins, D. Hanlon, N. Scheuschner, J. Maultzsch, L. Houben, G. S. Duesberg, J. F. Donegan, V. Nicolosi, J. N. Coleman, *Nature Commun.* **2014**, *5*, 4576.

[6] S. Grieger, B. M. Szydłowska, V. Rao, E. Steinmann, M. Dodds, Z. Gholamvand, G. S. Duesberg, J. Zaumseil, C. Backes, *Angew. Ch. Int. Ed.* **2020**, *59*, 13785-13792.

[7] a) H. Nan, Z. Wang, W. Wang, Z. Liang, Y. Lu, Q. Chen, D. He, P. Tan, F. Miao, X. Wang, J. Wang, Z. Ni, *ACS Nano* **2014**, *8*, 5738-5745; b) K. F. Mak, K. He, C. Lee, G. H. Lee, J. Hone, T. F. Heinz, J. Shan, *Nat. Mater.* **2013**, *12*, 207-211.

[8] a) R. C. Longo, R. Addou, S. Kc, J.-Y. Noh, C. M. Smyth, D. Barrera, C. Zhang, J. W. P. Hsu, R. M. Wallace, K. Cho, *2D Mater.* **2017**, *4*, 025050; b) V. Carozo, Y. Wang, K. Fujisawa, B. R. Carvalho, A. McCreary, S. Feng, Z. Lin, C. Zhou, N. Perea-López, A. L. Elías, B. Kabius, V. H. Crespi, M. Terrones, *Sci.Adv.* **2017**, *3*, e1602813.

[9] P. Atkin, D. W. M. Lau, Q. Zhang, C. Zheng, K. J. Berean, M. R. Field, J. Z. Ou, I. S. Cole, T. Daeneke, K. Kalantar-Zadeh, *2D Mater.* **2017**, *5*, 015013.

[10] P. Afanasiev, C. Lorentz, *J. Phys. Chem. C* **2019**, *123*, 7486-7494.

[11] D. Hanlon, C. Backes, E. Doherty, C. S. Cucinotta, N. C. Berner, C. Boland, K. Lee, P. Lynch, Z. Gholamvand, A. Harvey, S. Zhang, K. Wang, G. Moynihan, A. Pokle, Q. M. Ramasse, N. McEvoy, W. J. Blau, J. Wang, G. Abellan, F. Hauke, A. Hirsch, S. Sanvito, D. D. O'Regan, G. S. Duesberg, V. Nicolosi, J. N. Coleman, *Nature Commun.* **2015**, *6*, 8563.

[12] K. J. Laidler, in *Pure and Applied Chemistry, Vol. 68*, **1996**, p. 149.